POLITECNICO DI TORINO

Corso di Laurea Magistrale in Ingegneria Elettronica

Facoltà di Ingegneria

Master Thesis

Use of Flame Spray Pyrolysis for the Design of a 3D Plasmonic Resonant Metamaterial for the Optical Sensing of Volatile Compunds

Supervisors:

Prof. Matteo Cocuzza

Prof. Antonio Tricoli

Candidate:

Chiara Ricci

October 2018

Abstract

Localized Surface Plasmonic Resonance (LSPR) consists of collective oscillations of free electrons in noble material nanoparticles. This interesting phenomenon can be used in gas sensing applications due to variations of the refractive index of the surrounding environment and a strong local electric field. As a result, LSPR-based devices can be potentially suitable in the detection of small concentrations of different analytes. So far, several plasmonic structures have been implemented to improve both this capability of gas detection and a strong selectivity towards different analytes. Most of these aforementioned architectures are basically bilayered, but in this project a 3D metamaterial will be presented: thanks to an innovative sinthesis technique such as Double Spray Flame Pyrolysis (DSFP) one is able to fabricate a plasmonic resonant architecture in which plasmonic properties are exploited better than in bilayers and, consequently, enhanced performances are possible.

Master Thesis Project in Collaboration with the Australian National University (ANU)

Acknowledgements

It is with immense gratitude that I say thank you to my university Politecnico di Torino to have let me the chance to join this research project at the Australian National University, in particular thank you to my Italian supervisor Matteo Cocuzza. Really special thanks go to my Australian supervisors Antonio Tricoli and Zelio Fusco as they had the patience to teach me and mentor me in this new experience, and to all the fantastic people I had the pleasure to meet.
Thank you to my parents, my grandparents, my sister, my family and everyone that supported me and always believed in me. This means a lot to me.
I will never forget the people in *Campus SANPAOLO*, for the uncountable laughs and great time we shared, you are a second family to me.
Special mention to my special girls Gaia, Julie, Maria and Luisa, because even though we don't go out as much as we used to in high school we always help each other and support each other..you will always have my heart.
Another special mention for my *CNC* friends, because you make every summer memorable.
And last but absolutely not least, a huge thank you goes to Pierluigi Micarelli, the most supporting and lovely person I know: you are the best.

To the memory of my Grandmothers and Monica Di Carlo

Contents

Nomenclature

- *Greek symbols*

γ	: Damping element due to electron collisions
$\tilde{\epsilon}$	: Metal dielectric function
ϵ_d	: Real part of the metal dielectric function according to Drude model
ϵ_0	: permittivity in free space ($8.854x10^{-12}$ F/m)
ϵ_1	: Real part of the metal dielectric function
ϵ_2	: Imaginary part of the metal dielectric function
ϵ_m	: Dielectric function of the surrounding medium
λ	: Wavelength of the incident field
λ_{LSPR}	: Maximum wavelength peak
λ_p	: Wavelength corresponding to the plasma frequency
$\Delta\lambda$	: LSPR spectral shift
μ	: Center of the exponentially modified gaussian distribution function
σ	: Conductivity
σ_{sca}	: Scattering cross-section
σ_{ext}	: Extinction cross-section
σ_{abs}	: Absorption cross-section
ω	: Frequency
ω_{LSPR}	: Maximum frequency
ω_p	: Plasma frequency
Γ	: Gamma of the exponentially modified gaussian distribution function

- *Other symbols*

c : Light propagation velocity ($3x10^8$ m/s)
d : Particle's size
e : Electron's density
l_d : Electromagnetic field decay length expressed in nm
m_e : Electron's effective mass
m : Sensitivity factor in nm per refractive index unit (RIU)
n_{air} : Refractive index of the air in refractive index unit (RIU)
$n_{analyte}$: Refractive index of the external gas(es) in refractive index unit (RIU)
w : Sigma of the exponentially modified gaussian distribution function
A : Amplitude of the exponentially modified gaussian distribution function
N : Carrier density
S : Sensitivity
V : Volume of the particle

- *Symbols in Appendix*

ΔOD : Optical density
ΔT : Transmittance modulation
η : Colouration efficiency
λ : Operating wavelength
τ_{rec} : Recovery time or bleaching time
τ_{res} : Response time or coloration time
Q : Charge

List of Figures

List of Tables

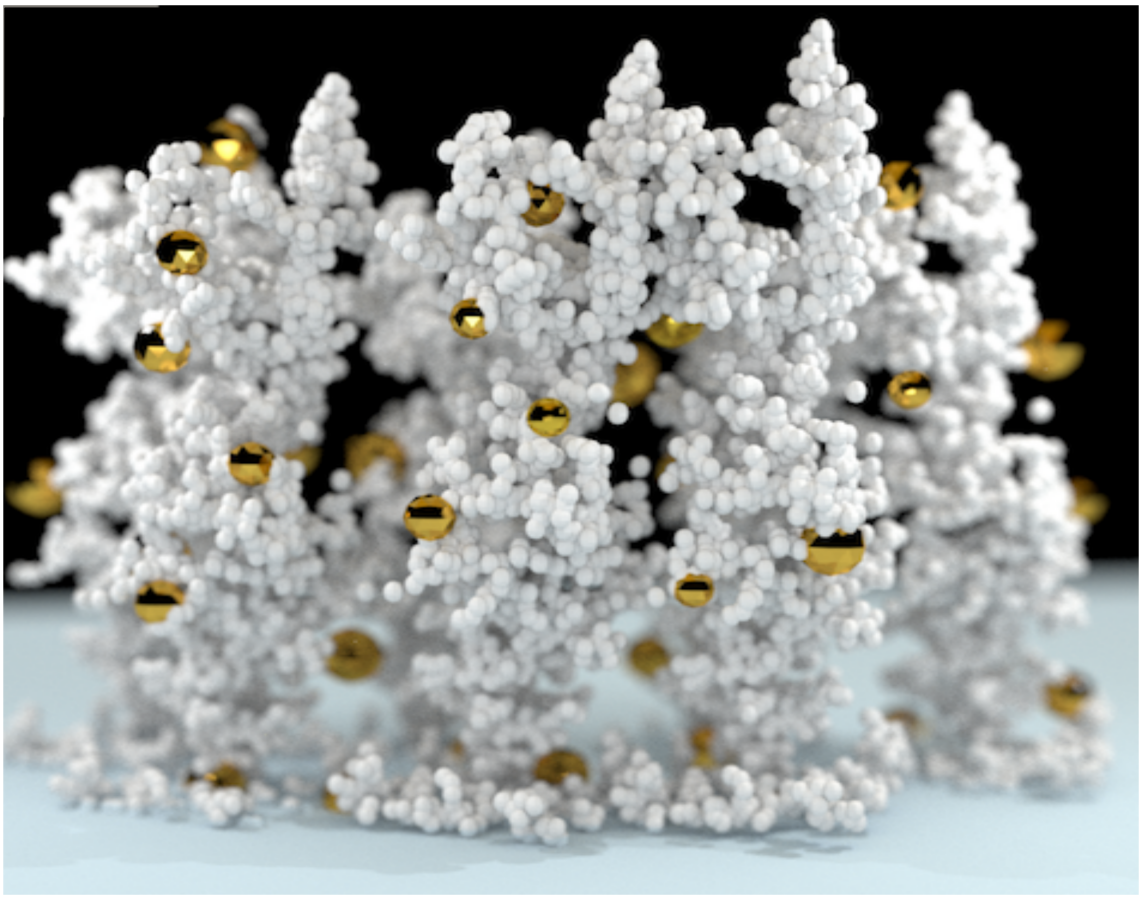

Figure 1. *Digital representation of a 3D metamaterial made of gold (yellow dots) and titanium oxide (in white). Courtesy of Co- Advisor Zelio Fusco*

Chapter 1

Introduction

Using miniaturized sensors in everyday life is something that grows so fast, as these are necessary to measure data for explaining phenomena of any kind. For this reason they find many applications such as robotics, cars, medicine, safety, defence, industry.
According mostly to the data they have to measure, sensors can be classified in several categories:

- **Temperature** sensors;
- **Pressure** sensors;
- **Force** sensors;
- **Electrochemical** sensors;
- **Gas** sensors;

and many others. This work will be focused on the last mentioned ones, gas sensors, mostly used for monitoring and detecting potentially hazardous chemicals and gases.
The basic principle is the same: once the device is exposed to some analyte, the sensor will change its physical properties. Depending on which physical properties are going to change it is possible to divide

them in other categories such as piezoresistive, chemiresistive or optical. Piezoresistive sensors will detect an analyte through a variation in electrical properties,while chemoresistive ones use a variation in the mass. Optical sensors will be investigated here, showing a change in their optical properties after the exposure of the device to the analyte. These are pretty new ones and thus still unexplored, but so far they have proved valid advantages such as simplicity in the equipment and in the measure procedure. The basic principle of an optical sensor is the so called "Localized Surface Plasmonic Resonance" (LSPR), efficient in the selective detection of volatile organic compounds (VOCs) in the atmosphere.

Generally speaking, a plasmon is a quantized and collective oscillation of free electrons against the fixed positively charged nuclei in a metal, which can be resonantly driven by an external electromagnetic field, [1], [2]. Thus, plasmonic resonance takes place when a photon interacts with a metallic material that lets electrons move coherently resonating all at the same wavelength. This resonance due to these collective oscillation will enhance enormously the electric field but only in the near field. This enhancement is thus very localized: as soon as one moves apart from the minimum distance of the metal the enhancement factor will decrease drastically in intensity, of several orders of magnitude.

Plasmonic theory has been developed by Gustav Mie, who solved Maxwell equations using the Drude model for metals and ended up with extinction cross section, scattering cross section and absorption cross section functions. Extinction cross section, defined as the summation of absorption and scattering cross sections, represents the exact solution of Maxwell equations in the assumption of perfectly spherical

nanoparticles with dimensions much smaller than the wavelength of the incident light. Whenever the dimensions change it is important to take into account some other effects such as electron collisions so the profile of the plasmonic resonance and their wavelength will change for a certain amount. There is, then, a dependency of the cross section on the medium volume or, in other words, on the size and shape of the metal and a high sensibility to the local environment. This happens because the solutions of Mie's theory (i.e. extintion cross section, scattering cross section, absorption cross section) depend on the permittivity of the metal and permettivity of the medium which are related to refractive index by a square root, so even a small change in the permittivity of the medium leads to a plasmonic shift. This is very important when performing sensing of plasmonic nanostructures.

Many research groups are trying to improve the plasmonic near field through really precise litographic structures, but all the methods adopted so far are prevalently used for planar structures. Nowadays it could be challenging to overcome bidimensionality and pave the way towards 3D structures, that would be useful for several applications.
A big effort has been made in the fabrication of 3D plasmonic resonant structures and these are called metamaterials. This marks a neat distinction between metasurfaces (which deal with 2D) and metamaterials (which work in 3D). There is not a real exact definition of metamaterial, but they can be conveniently defined as subwavelength structures that have some reproducible properties: 3D metamaterial is something that has 3D arrangement so it does not lie on a surface and it is still subwavelength, thus it can resonate or confine electromagnetic wavelength on a volume which is much smaller than the interactive wavelength to which the structure is exposed.
Even if this can be considered a good definition for metamaterial the

topic is still controversial, but as long as visible properties in three dimensions are verified it is possible to talk about metamaterials. There are different ways to fabricate them, the most common is the lithographic process but has some limitations: it is expensive, time consuming and the maximum number of layer that can be possible to stack on top of each other is limited, even though good resolution and high precision are possible. This means that lithographic architectures are very wide but the height is very small and consequently the volume is small. Self assembly can be a possible solution too, but it lacks in controlling the distribution of nanoparticles, so it is good for microwave applications and not for optical ones.

In this work it is implemented an aerosol synthesis with flame spray pyrolysis to create a 3D resonant metamaterial in which TiO_2 nanoparticles will be used as a scaffold and at the same time Au nanoparticles will be deposited: the porosity of the dielectric material will be exploited to enhance the plasmonic volume, so instead of dealing with a 2D bilayer, the gold nanoparticles will be spread all around the titanium oxide. Most importantly flame spray is a quick process, feasible on large scale as well as scalable. After an optimization of the flame setup itself, and due to the proper nucleation of the particles during growth, samples will look uniform.

Finite Domain Time Domain (FDTD) simulations will be added too, not only for a theoretical understanding purpose, but also in order to show the behavior of a real cluster of TiO_2 and gold nanospheres with dimension taken according to the sample's caracterization (i.e. XRD, SEM and TEM images). The same kind of simulations are computed also for a bilayered structure having the same initial conditions: it will be shown that the normalized electric field enhancement due to the plasmonic resonance is much higher in the 3D architecture rather

than a 2D metasurface.

Confident with these improvements, optical gas sensing tests are performed, so basically every sample is exposed to different cycles of different concentrations of some gases. The results are challenging, because a lower limit of detection will be found.

After this brief introduction, this work will be organized as follows: Chapter 2 will illustrate how LSPR works from a theoretical point of view, while Chapter 3 will study and analyse the evolution of spray flame pyrolysis technique. Chapters 4 and 5 will show and comment all the results coming from the sensing tests and simulations, while finally Chapter 6 will give some final considerations and conclusions. There is also Appendix that will illustrate othere applications coming from the use of flame spray pyrolysis technique.

Chapter 2

Plasmonic sensing

The utilization of optical sensors for medical diagnosis and monitoring of diseases, detection of environmental pollutants and biological agents is increasing more and more in the last decade. Optical sensors exploit various techniques such as fluorescence, light absorption or scattering, [1], but one of the most promising is the localized surface plasmonic resonance technique (LSPR) that can detect chemical and biological targets at nanoscale. Such sensors take advantage of typical properties of noble metal nanoparticles of having a collective oscillation of the conduction electrons if an incident photon shows a certain frequency called resonance frequency. This depends on many factors such as size, shape, dielectric properties both of the material and of the external environment.
Their improvement with respect to other kind of sensors such as chemoresistive, is their capability to operate even at room temperature, thus simple laboratory equipment is required. This means also that real-time measurements are possible, without the need to wait for the sensor's stabilization. At the same time, LSPR-based sensors still show low sensitivity to the different analytes, which is one of the main goals that have to be achieved.

In this chapter LSPR will be analyzed from a theoretical point of

view, while the realization, optimization and tests will be described in the next chapters.

2.1 From Surface Plasmon to Localized Surface Plasmon

A plasmon is a collective oscillation of free electrons in a metal: if an external electric field, having a certain frequency called *plasma frequency* or *resonance frequency*, excites the external electrons of a metal, then a displacement of electron gas with respect to the ionic cores takes place, [2].
The simplest plasmonic system is the so-called surface plasmon, represented by the interface between a metal and a dielectric where the real part of the dielectric function has opposite sign with respect to the metal one, [3]. Surface plasmons interact with photons to form coupled waves called surface plasmon polaritons (SPPs) that propagate along the length of the metal: the field of the SPP wave is supposed to travel at the metal-dielectric interface, so it is stronger at the interface and decays in both the metal and the dielectric, as shown schematically in Figure 2.1:

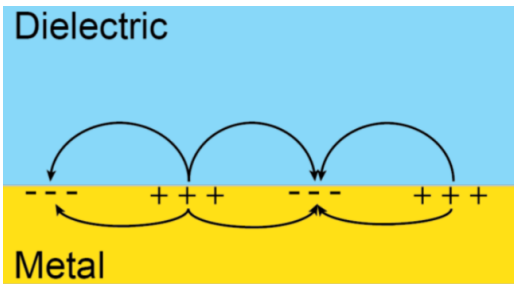

Figure 2.1. *Scheme of surface plasmon polariton, [4]*

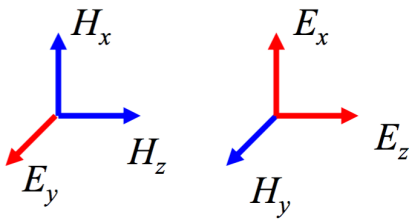

Figure 2.2. *Schematic of propagating TE and TM modes, [5]*

Solving Maxwell equations it turns out that for TE modes (Figure

2.2 for reference) E_y is continuous at the interface due to boundary conditions and also its derivative in x is. But since we expect that the distribution is not differentiable in x = 0, TE mode cannot be used. For TM mode (Figure 2.2 for reference), instead, it turns out that H_y is continuous at the interface due to boundary conditions, but it may have discontinuities in the first derivative in x which works really well for the scope. As a result, plasmonic waveguides are polarization sensitive and in particular only TM modes can be exploited. In addition, it can be demonstrated that plasmonic waveguides are feasible if and only if one of the media (the metal) has a negative epsilon real part, [5]. However, due to its very small wavelength, SPPs can only be optically excited using special configurations to match the momentum of surface plasmons with that of the incident photons. One of the most widely used methods involves using a prism to match the phase of the incoming wave with that of the SPP wave, [6], [7].
When a surface plasmon is confined to a particle of a size much smaller than the wavelength of the incident light it is possible to talk about *nanoparticle* structure. In this case the external free electrons of the particle participate in the collective oscillation (Figure 2.3), and when the frequency of the incident photon is close to the oscillation frequency of these electrons in the nanoparticle then Localized Surface Plasmon Resonance (LSPR) takes place. This is schematically shown in Figure 2.4:

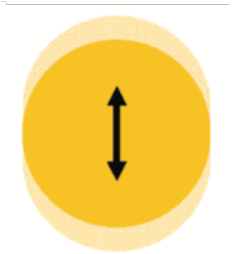

Figure 2.3. *A localized surface plasmon, [2]*

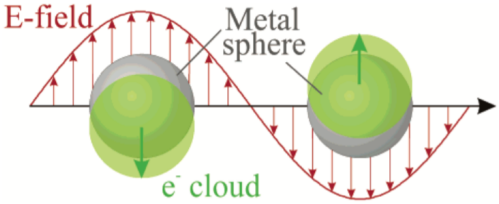

Figure 2.4. *Schematic of plasmon oscillation, [11]*

In Localised Surdace Plasmons (LSPs) the electric field near the particle's surface is enhanced and rapidly decays with the distance from the nanoparticles' surface, typically within of the order of nanometers, [8], [9], specifically within the first 6-30 nm, [10]. The particle's extinction, which represents the summation of absorption and scattering cross section of the material after the impact of the incident light, has a maximum at the plasmon resonance frequency, which is proportional to the wavelength. For noble metal nanoparticles this maximum occurs at visible wavelengths.

2.2 Localized surface plasmon resonance (LSPR)

LSPR involves a noble metal nanoparticle and creates an absorption and scattering peak after the emission of an electric field: in resonance conditions induced electric dipoles appear, the local electric field increases abruptly giving high scattering and, consuequently, high extinction peaks. This can be useful for the detection of molecular interactions near the nanoparticle surface through shifts in the LSPR spectral peak, [2]. Also, this explains why the particle's optical extinction has a maximum at the plasmon resonance frequency, as already mentioned in in Section 2.1. This extinction peak depends mainly on the refractive index of the surrounding medium, this is the reason why

LSPR-based sensor can be useful for monitoring and detection.

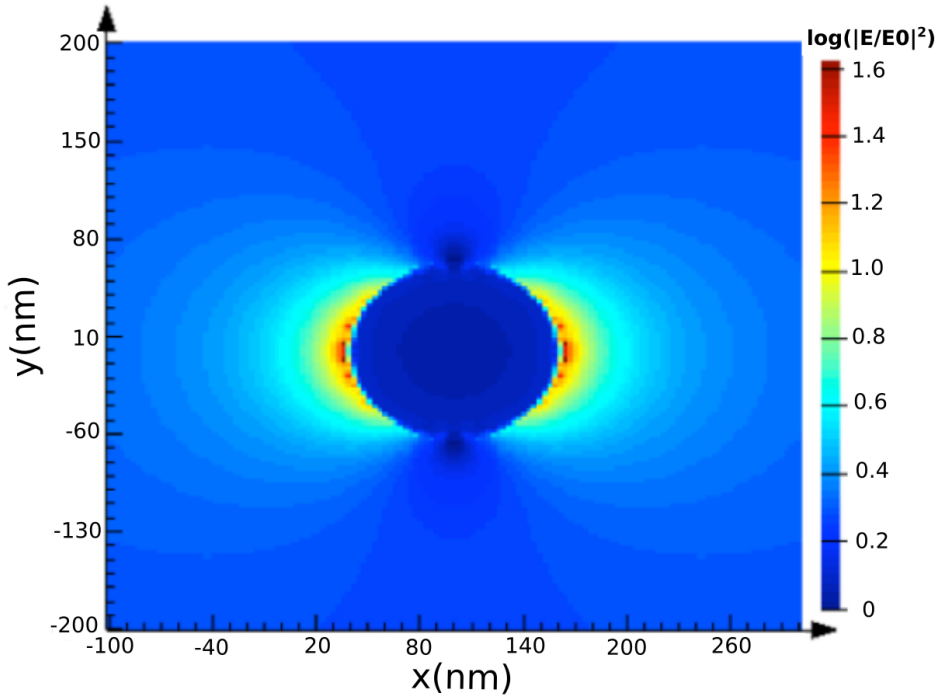

Figure 2.5. *Simulation of plasmonic effect on a 85nm radius gold sphere using Lumerical FDTD Solutions*

To relate the dipole plasmon frequency of a metal nanoparticle to the dielectric constant, we consider the interaction of light with a spherical particle much smaller than the wavelength of light so that the electric field of the light can be considered constant, and operating in *quasi static* approximation is possible, [11]. Supposed to have an incident electric field, by solving LaPlace's equation one finds the electromagnetic field surrounding the particle, which turns out to be spherical harmonics. If one considers only the first harmonic, it can be noticed that the electromagnetic field is proportional to the applied incident field and to the induced dipole field that results from polarization of the conduction electron density, [11].

2.2.1 Mie's theory

In order to better understand LSPR, it is better to recall Mie's theory formulated in the early 20th century and precisely in 1908, [11]. It provides an exact solution to Maxwell equations for the scattering and absorption of light by *spherical* particles, but it is fairly suitable for similar geometries. For very small particles, for which d << λ (meaning that the size of the particle is much smaller than the wavelength of the incident field), the interaction between a particle and the electric field can be explained by the *quasi-static* approximation as already explained previously, while for bigger sizes (d < λ) Mie's theory should be used.
Starting from the general expressions of scattering, absorption, extinction cross-sections and given $\tilde{\epsilon} = \epsilon_1 + i\epsilon_2$ as the dielectric function of the metal, [2], one can find (for the symbol's legend please look at the Nomenclature page):

$$\sigma_{ext} = \frac{18\pi\epsilon_m^{3/2}V}{\lambda}\frac{\epsilon_2(\lambda)}{[\epsilon_1(\lambda)+2\epsilon_m]^2+\epsilon_2(\lambda)^2} \tag{2.1}$$

$$\sigma_{sca} = \frac{32\pi^4\epsilon_m^2V^2}{\lambda^4}\frac{[\epsilon_1(\lambda)-\epsilon_m]^2+[\epsilon_2(\lambda)]^2}{[\epsilon_1(\lambda)+2\epsilon_m]^2+[\epsilon_2(\lambda)]^2} \tag{2.2}$$

$$\sigma_{abs} = \sigma_{ext} - \sigma_{sca} \tag{2.3}$$

In order to have an extinction cross section maximized (eq. 2.1), the denominator should be minimized. This is possible only if ϵ_1 = -2ϵ_m, which is the reason why the LSPR extinction peak depends on the external environment. Remember that this is true for spheroidal shapes, as the structure of the particle plays an important role in LSPR.

In order to find the functional relation between the LSPR peak wavelength and the dielectric function of the surrounding medium, one can use the Drude model for the metal dielectric constant, [2], [5], [12], which is the expression for electric permittivity in conducting media:

$$\tilde{\epsilon}(\omega) = \epsilon_d - i\frac{\sigma}{\omega} \tag{2.4}$$

From equation 2.4 one can explicit the real part of the metal dielectric function as follows, [2], [12]:

$$\epsilon_1 = 1 - \frac{\omega_p^2}{\omega^2 + \gamma^2} \tag{2.5}$$

with γ the damping constant due to electron collision, and ω_p the plasma frequency defined as follows:

$$\omega_p = \sqrt{\frac{Ne^2}{m_e \epsilon_0}} \tag{2.6}$$

Given the maximum value of ϵ_1 (=-2ϵ_m), the maximum frequency is obtained:

$$\omega_{LSPR} = \frac{\omega_p}{\sqrt{2\epsilon_m + 1}} \tag{2.7}$$

which in terms of wavelength ($\lambda = 2\pi c/\omega$) and refractive index ($\epsilon_m = n_m^2$) the wavelength peak is easily computed:

$$\lambda_{LSPR} = \lambda_p \sqrt{2n_m^2 + 1} \tag{2.8}$$

with

$$\lambda_p = \frac{2\pi c}{\omega_p} \sqrt{\frac{4\pi^2 c^2 m \epsilon_0}{Ne^2}} \tag{2.9}$$

where an almost linear dependency between the LSPR peak wavelength and the refractive index should be noticed.

As Mie's theory gives exact solution only for spherical particles, an indicative formula suitable for every other geometry should have been provided. For this reason, in later years, an empirical formula for the LSPR spectral shift $d\lambda$ as a function of the variation of the refractive index is found to be, [13]:

$$d\lambda_p \approx S(n_{air} - n_{analyte})(1 - e^{\frac{-2d}{l_d}}) \tag{2.10}$$

where:

- S is the sensitivity and depends on many factors such as material's choice, its structure and its size, [13]. In particular, from this parameter one can determine how much particles per million (ppm) can be detected. The main goal should be to optimize it as much as possible, as precision and accuracy depend on it;
- $(n_{air} - n_{analyte})$ underlines the dependency of the spectral shift on the refractive indexes of the gases (linear dependence as in equation 2.8), because if it changes, then shifts of the extinction peak are observed;
- $(1 - e^{\frac{-2d}{l_d}})$ takes into account the field propagation, and it means that it decays rapidly when it reaches long distances. Thus, this is a very localized field enhancement.

Clearly, this shift relies on many physical factors such as size, structure and dielectric properties, related to the material as well as the external environment in which the nanoparticle is. Kelly et al., [11] pointed out that even the substrate affects plasmon resonance properties.

The dependence of LSPR wavelength on size and dielectric properties of the nanoparticles can be seen in equations 2.1 and 2.2 from Mie's theory, but it is the dependence on the dielectric property of the surrounding media that makes LSPs useful as sensors for a pletora of applications, including environmental monitoring, safety, process control and medical diagnostics, [14]. This is possible because when an external electric field around a nanoparticle is present, the polarization of the sorrounding media is induced, [4].
Another issue concerns the dependence of the nanoparticle shape, as Mie theory gives an exact analytical solution of Maxwell's equations for spherical ones. Recently, progresses have been made also in the computation of an (almost) exact solution for nonspherical particles, showing that the plasmon resonance changes behavior as the particle becomes more or less oblate, or even if the particle is prolate, [9], [11]. According to theoretical simulations and experimental data, anisotropic nanostructures exhibit higher refractive index sensitivity than spherical nanoparticles. The refractive index sensitivity of gold nanorods, in particular, is typically around 250nm/RIU, whereas the refractive index sensitivity is around 60 nm/RIU for nanospheres, [9]. Nanostructures of other shapes, including nanocubes, nanoshells, nanodiscs, nanotriangles, nanostars, nanobipyramids, have also been investigated and explored, [1], [9], [11].

2.2.2 LSPR-based sensors

The idea of LSPR sensors is to exploit the spectral shift or resonance linewidth $d\lambda_p$ in order to recognize whether a gas different from air is present in the external environment, [1], [12], [13]. What makes them really promising is the capability to operate at room temperature, which would make them fairly practical as they require common

laboratory equipment and therefore are often cost-effective. In addition they are immediately ready for use and do not require such a long time for a response: it was proved that LSPR can be promising in sensing volatile organic compounds (VOCs) in gaseous form with a fast and reversible response. In addition, they can generate chemical selectivity, [15].
Through extinction measurements as shown in Figure 2.6 and according to equation 2.10 one can detect spectral shifts.

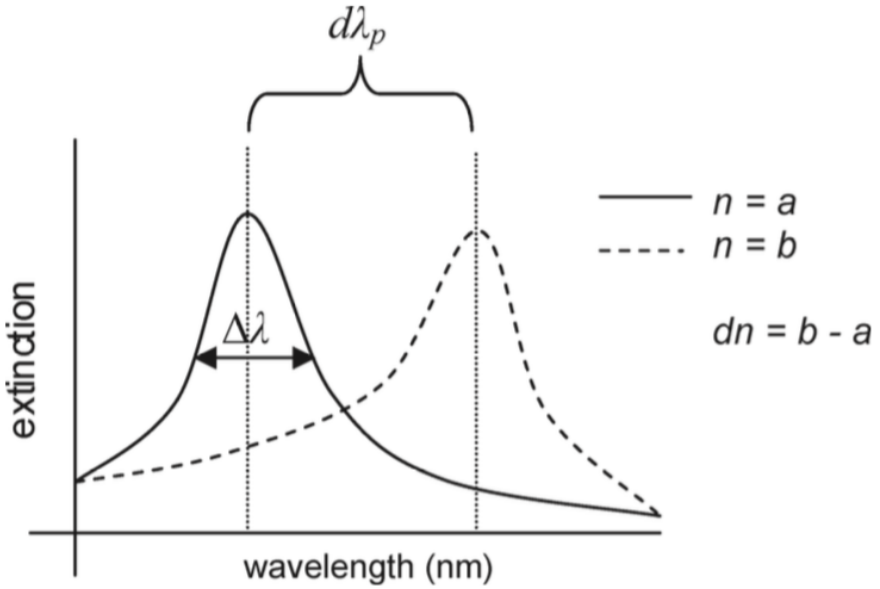

Figure 2.6. *Scattering spectrum for the plasmonic system after a change of the refractive index in the environment, [1]. $d\lambda_p$ represents the resonance linewidth, $\Delta\lambda$ is the so called full width at half maximum (FWHM) and dn is the refractive index variation*

As already seen in equations 2.8 and 2.10 the dependency between the LSPR shift and the refractive index is approximately linear, and the refractive index sensitivity can be rewritten as follows:

$$S = \frac{d\lambda_p}{dn} \tag{2.11}$$

Indeed, in order to quantify the sensing performance of a plasmonic system, one can consider this parameter S, defined as the peak shift of the plasmonic resonance (usually in nm) per refractive index unit (RIU) as it will be shown in equation 2.11, [16]. However, since the accuracy of the peak tracking depends both on the magnitude of the peak shift and on the resonance linewidth, a more suitable choice for plasmonic systems is the figure of merit (FOM), obtained by dividing the refractive index sensitivity by $\Delta\lambda$ which is the full width at half maximum (FWHM) of the resonance, [1]:

$$FOM = \frac{S}{\Delta\lambda} \tag{2.12}$$

Thus, there are two key approaches for optimizing the figure of merit in a plasmonic sensing geometry: reducing the resonance linewidth (or FWHM), and increasing the peak shift through a local field-enhancement. In general, plasmon oscillations in nanoparticles experience damping arising from two contributions: intrinsic damping due to electron-electron collisions and impurity scattering in the metal, as well as radiation damping due to the direct decay of the collective oscillations into photons.

LSPR is theoretically possible in any metal, alloy or semiconductor with a large negative real dielectric constant and small imaginary dielectric constant, [9], [13], but utilizing noble metals for the resonant nano particles helps to reduce intrinsic damping. In addition, for noble metals LSPR wavelengths fall in the visible region of the electromagnetic spectra, making them easily accessible. This is the reason why they are very used for this purpose. Gold and silver are the two most common and suitable noble metals for LSPR-based sensors, but other relevant metals or metal oxides used in this field are for example copper, palladium, alumina and zinc oxide [1], [9], [13]. However,

non-noble metals are susceptible to corrosion in aqueous environments and oxidation in air, reducing the refractive index sensitivity. Silver, due to its high reactivity and losses, [1], [9] is less preferred than gold, which is oxidation resistant, stable and easy to work with. This makes gold more efficient too.

Many effective methods have been tried for sensitivity enhancement such as molecularly imprinted polymer (MIP) [15], Antibody—antigen—antibody sandwich assay format, Au-nanoparticles-labelled antibody, or 3D assembly of metallic nanostructures, [9].

One of the main goals of LSPR sensing is the detection of volatile organic compounds (VOCs) in gaseous form and, as already mentioned in previous section, this can be used in so many applications. Some examples are pH sensing, medical diagnostics, [10], [17], biological purposes, [10], [14]. Particularly interesting is the detection of VOCs for non invasive medical diagnostic by breath analysis.
Human breath is basically a mixture of nitrogen, oxygen, carbon dioxide, water, and inert gases. There is, however, a remaining small fraction made of more than 1000 volatile organic compounds (VOCs) with concentrations from parts per million (ppm) to parts per trillion (ppt) by volume, [18]. Some of this VOCs such as acetone, ethanol, ammonia, pentane, toluene, has been successfully identified as breath markers for several diseases, meaning that an excess of their quantity in the human breath may be associated to one of them.
Optical sensor do not reach very low concentration of molecules because their sensitivity is still poor, so working on complex systems such as human breath is still not feasible. Working on the sensitivity, although, can be challenging and make this study in the next future possible.
In this work an optical sensor made of gold (Au) nanoparticles (as

noble metal) and porous titanium dioxide (TiO_2) was fabricated and tested under the presence of ethanol, toluene and acetone, as these compounds are considered as markers for diabetes (acetone) and lung cancer diseases (toluene, ethanol), [18], [19]. The idea of using titanium dioxide fractals comes from their low effective refractive index that minimizes the attenuation of the optical signal, [10] and the capability of trapping the gas molecules for an improvement in the interaction with the plasmonic field, thus a better optical response and a better sensitivity.
The fractals were directly self-assembled on the substrate via direct deposition of flame-made TiO_2 nanoparticle aerosols in the diffusion regime.

2.3 Preliminary Analysis

Before the samples are being characterized, some very preliminary electrodynamic simulations based on Finite-Difference Time-Domain (FDTD) method are carried in order to predict what the future behavior will be. For this purpose Lumerical FDTD Solutions software will be used. Drude models are applied to TiO_2, while the optical properties of Au are taken from the Johnson and Christy, [10]. Perfectly matched layers were employed as boundary conditions to avoid the wave reflection at the boundary. Concerning the geometry, a box having dimensions of 200x200x200 nm^3 is employed to represent the scaffold of TiO_2, into which small spheres of Au having diameter of 50 nm are inserted randomly. The final architecture is shown in Figure 2.7, and from this final plots are obtained.

The only goal of these first simulations is just to have an idea of the overall plasmonic phenomenon, so please note that every parameter is set according to the literature and to what one expects to obtain from a real metamaterial.

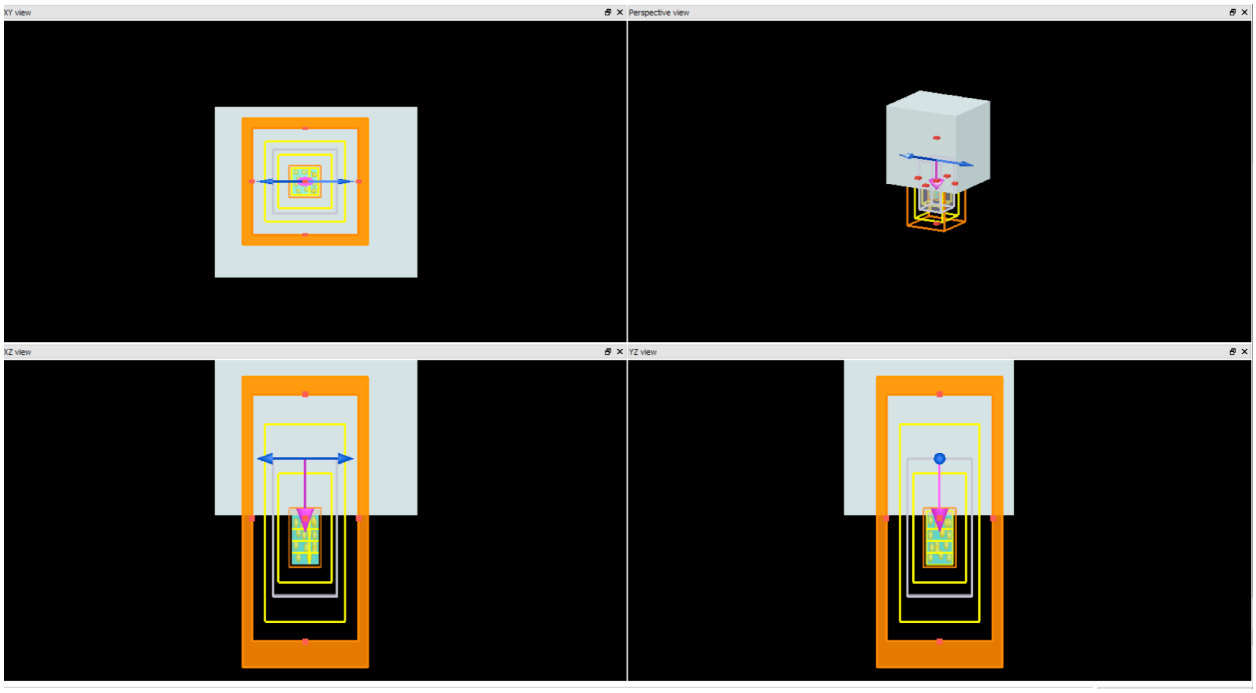

Figure 2.7. *Geometry settings with Lumerical FDTD Solutions: top view (top left), overall view (top right), front view (bottom left), lateral view (bottom right)*

2.3.1 Porosity Level

The main advantage of having a cloud of TiO_2 around Au nanoparticles is the capability to enhance drastically the plasmonic electric field with respect to the bare gold. So according to what should be expected, the first simulations were about finding out the best porosity level. Three tests were made, 15 gold spheres having 50 nm diameter immersed in TiO_2 with 70%, 90% and 95% porosity respesctively. The results are shown in Figures 2.8, 2.9, 2.10 respectively:

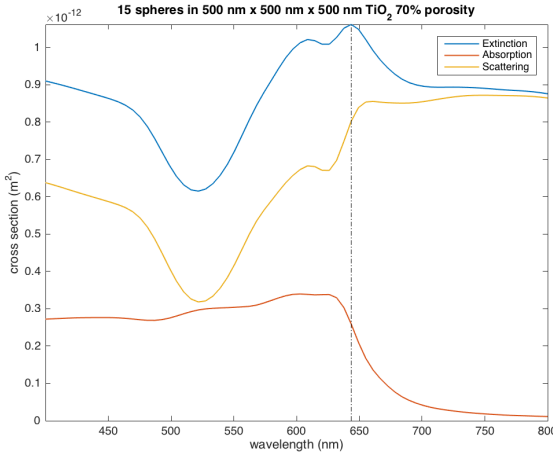

Figure 2.8. *Cross sections with 70% porosity*

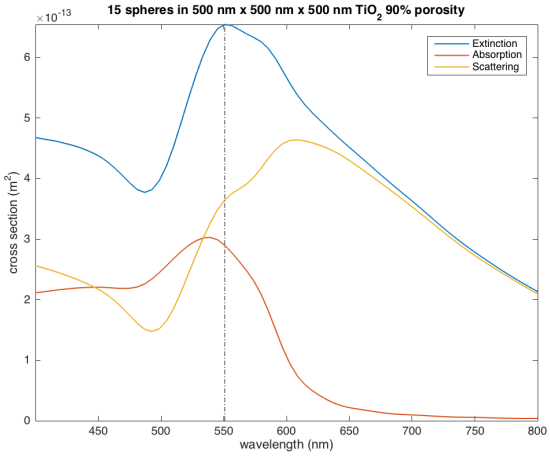

Figure 2.9. *Cross sections with 90% porosity*

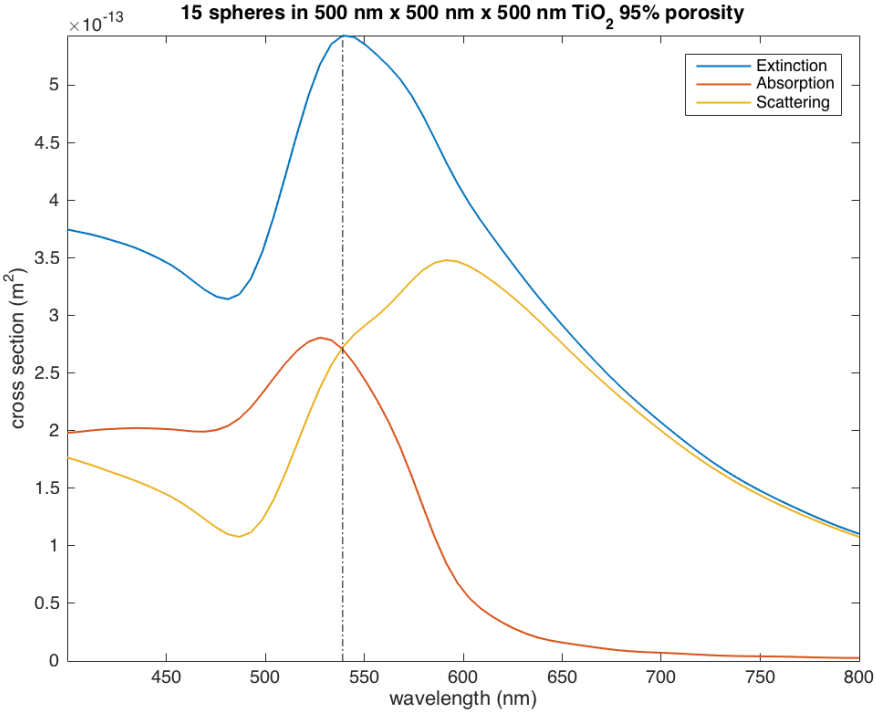

Figure 2.10. *Cross sections with 95% porosity*

At a first glance, the best results seem the ones with 90% and 95% porosity, as in both cases the extinction peak falls in the visible region while in the 70% porosity this does not happen. However, even though the case of 90% satisfies all the requirements for having a good shift enhancement such as resonance peak at visible length, high intensity and sharp profile, the most appropriate solutions is the case of 95% (Figure 2.10): here, the resonance peak is still at visible wavelength, but the extinction profile is sharper. To make sure this is the best options, one can compute the full width at half maximum (FWHM) of the extinction peak: with the help of OriginLab8 one can be able to take this curve and fit it to a known distribution, in this case an exponentially modified Gaussian distribution, characterized by the following expression, [20]:

$$f(x, A, \mu, w, \Gamma) = \frac{A\Gamma}{2} \exp[\Gamma(\mu - x + \Gamma\sigma^2/2)] erfc(\frac{\mu + \Gamma w^2 - x}{\sqrt{2}w}) \tag{2.13}$$

with $erfc$ complementary error function. FWHM can be computed as, [20]:

$$FWHM \approx 2w\sqrt{2ln2} \approx 2.3548w \tag{2.14}$$

It turns out that $w = 24.296$ for the 90% porosity case, and $w = 22.247$ for the 95% porosity case: for this reason this last case will be considered the best one.

2.3.2 Number of Spheres

Another issue is about the optimal number of spheres per 200x200x200 nm^3 volume for which the best results can be obtained. So in this case porosity and dimensions of the geometry were fixed, the number of gold spheres was first set to 5, then 10, 15 and finally 20. Figures

2.11, 2.12, 2.13 show results for 5, 10 and 20 spheres respectively, while results for 15 sphere was previously reported in Figure 2.10:

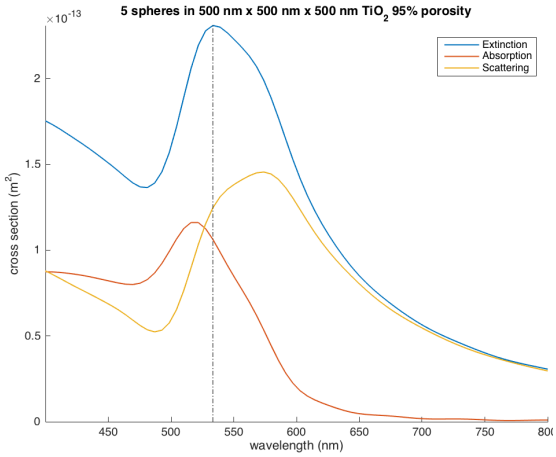

Figure 2.11. *Cross sections with 95% porosity and 5 spheres*

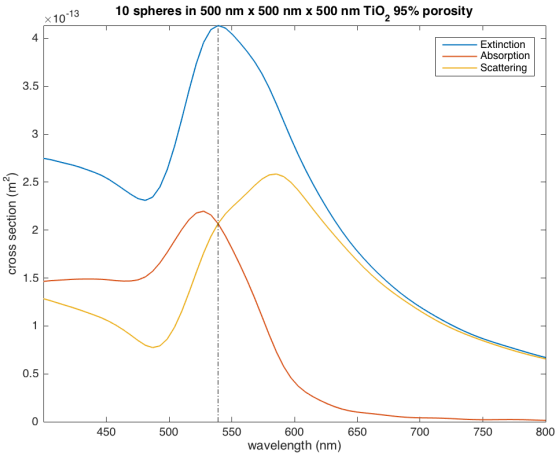

Figure 2.12. *Cross sections with 95% porosity and 10 spheres*

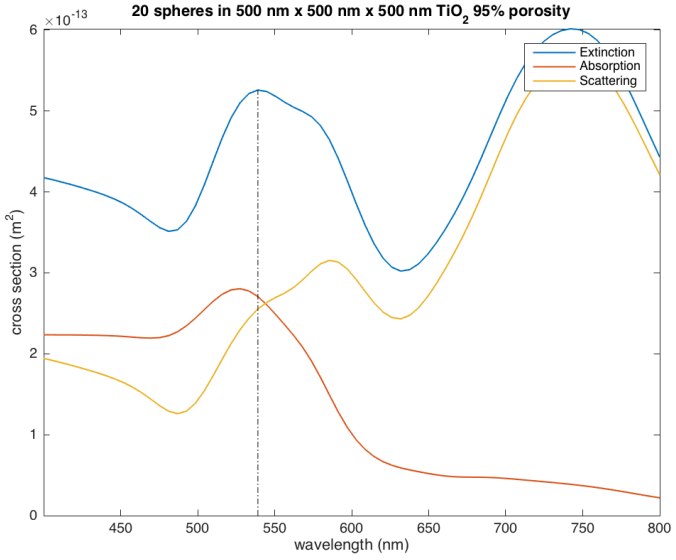

Figure 2.13. *Cross sections with 95% porosity and 20 spheres*

2.3.3 FWHM

Again the full width at half maximum (FWHM) is computed through OriginLab 8 always using an Exponentially Modified Gaussian distribution as fittng function, [20]. Remember FWHM values are computed using Equation 2.14. Final results are below in Table 2.1 and plotted in Figure 2.14, [20]:

Number of spheres	w	FWHM (nm)
5	24.6145	57.9622
10	23.8333	56.1226
15	22.2467	52.3866
20	32.0900	75.5650

Table 2.1. FWHM computation according to the number of spheres

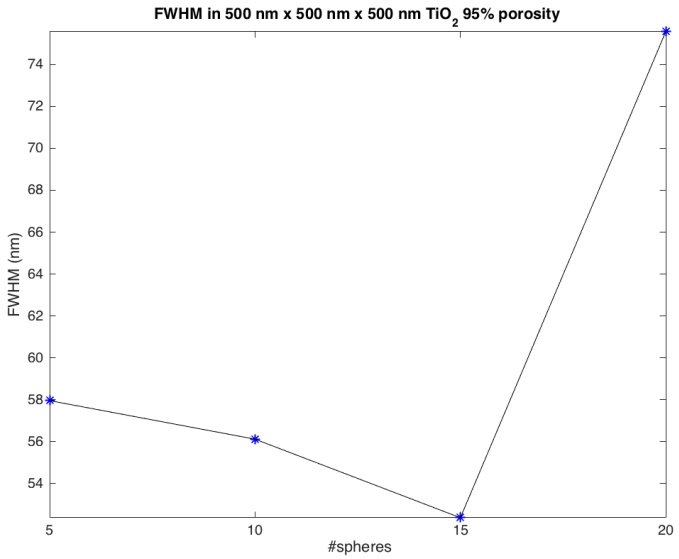

Figure 2.14. *Plot of FWHM for each test*

This means, from Figure 2.14, that the extinction profile peak is sharper as the number of spheres increases from 5 to 15, but becomes broader again when the number of spheres reaches 20. This proves

again the efficiency of having 15 spheres since a sharp, defined and recognizable peak is preferred when, in optical sensing, one deals with peak shifts. It is reasonable to suppose that too much spheres would mean bad coupling among the spheres and consequently a bad plasmonic performance.

2.3.4 Electric Field

In order to practically figure the working mechanism out, the electric field behavior of such structure (a 98% porous TiO_2 with 15 Au spheres randomly distributed in it)is shown Figure 2.15.
By arranging multiple plasmonic particles into a defined geometry, coupling effects may happen and can significantly improve the performances: the coupling of two modes can lead to a narrow spectral feature in the dipolar lineshape, giving a greatly increased FOM compared to simple dipolar plasmonic structures in the same spectral range. When decreasing the distance between the two rods, the electromagnetic fields can be confined to a progressively smaller volume, but leading to extremely high enhancement factors, only limited by fabrication, [16].
So when different nanoparticle interact with each others additional enhancements can arise. In that case the electromagnetic fields derived from the surface plasmon of individual nanoparticles may be affected by the dipolar interaction of neighbouring particles, resulting in significant changes in both the plasmon resonance extinction and scattering spectra. This near-field-coupling-induced peak shift is highly dependent on the interparticle distance, [9].
As the interparticle gap becomes smaller, larger coupling will be achieved; the coupling decays exponentially with an increasing interparticle gap. For this reason, in Figure 2.15 some red spots appear, meaning that around that nanoparticle the local electric field is increased due to the

coupling with neighbor ones.

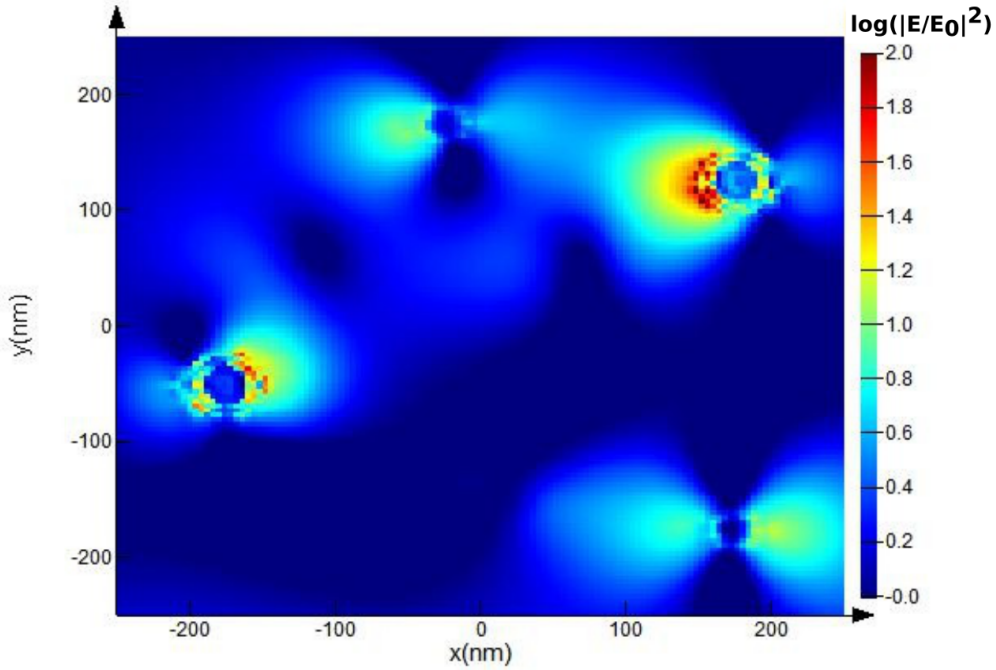

Figure 2.15. *Logarithmic squared absolute value behavior of the near electric field in the ideal case of 15 Au spheres immersed in a scaffold of* TiO_2

Chapter 3

Design and Techniques

In order to realize a semiconductor metal oxide (SMOX) based detector for gas sensors many techniques can be adopted, such as chemical vapor deposition (CVD) methods, [14], self assembly or litography, [1], [14]. For synthesis of highly porous films, aerosol technology is instead more attractive due to the versatility in nanoparticles' production, [21], [22], high film porosity percentage (95–98%), [10], [21], [23], and low cost, [21], [23].
Flame Spray Pyrolysis (FSP), in particular, is a high temperature aerosol technique for synthesizing nano-sized metal oxide catalysts of almost all metals by gas-to-particle conversion, [24]: it consists of dispersion, ignition and combustion of a metal containing (combustible) precursor liquid solution, [22], [25]. After evaporation and conversion of the metal precursor, particles are formed in the gas phase.
Flame-made nanoparticles have already shown efficient performances as gas sensors [17], [18], [26], functional coatings [26], UV photodetectors, [23], tissue engineering, [17], [27] and battery electrodes, [23].
However, specific designs of multi-component catalysts and the controlled dispersion of catalytic material on the support are limited with FSP. Double Flame Spray Pyrolysis (DFSP) overcomes this limit by burning individual metal oxide precursors in two opposing nozzles and

intersecting the flames at a defined temperature, and at a certain angle [24]. Both these parameter affect significantly the final result.
Porous film morphologies are the most common for semiconductor gas sensors and can be obtained by several methods such as spray pyrolysis, pulsed laser deposition and sputtering, but most of them can produce semiconductor films with relatively good control of single properties and only a few can control independently film thickness, grain, and crystal size. Therefore a porous film contains both multicrystalline grains and monocrystalline grains, one acts as dense film while the other as a particulate film. The sensitivity of such porous films towards an analyte and the optimal thickness of such a film depends on the respective fractions of dense and particulate components, [14].
As already mentioned in previous section, in this work a LSPR sensor made of gold nanoparticles surrounded by a porous titanium oxide cloud is fabricated, creating a so-called 3D resonant metamaterial. Gold is the noble metal that, as already mentioned in Chapter 2, will be adopted because in a noble metal any shift of the plasmonic peak in the extinction cross section occurs at visible wavelength. The presence of titanium oxide all around the gold nanoparticles, instead, makes sure that the plasmonic effect of gold is improved in all directions, and not only in part of it as it happens for planar structures (also called metasurfaces) where gold is previously deposited alone on the substrate. The final self-assembled porous metamaterial, in conclusion, provides enhanced performances: the higher the porosity of the porous cluster is, the easier the penetration of the field in the TiO_2 layer, [10].

3.1 Single Flame Spray Pyrolysis (SFSP)

Flame Spray Pyrolysis shows better performance than conventional techniques for SMOX-based sensors as it may provide highly christalline materials with large external surfaces areas and high temperature stability, [25], all in a single step. Moreover, it is able to produce fully porous films without dense regions. It is a process based on liquid precursors that flow through a two-fluid nozzle that uses high gas velocities to convert the liquid into fine droplets. As it can be seen (Figure 3.1), the structure is very simple: through a syringe, the precursor is injected into the main tube while the dispersion gas (O_2) flows into the secondary tubes. Around the nozzle there are supporting flames obtained by the injection of O_2 and CH_4. Both the nozzle and the supporting flames are controlled by mass flow controllers. Nanoparticles are collected from the gas-phase on water-cooled glass-fiber filters placed above the flame. Please note that the water-cooled substrate holder had the purpose to keep the substrate temperature below 150°C and avoid damages.

The liquid precursor (a mixture of organic solvents and metal organic precursors) carries all the energy into the flame. The composition, size and porosity of the resulting nanoparticles can be controlled with the temperature profile of the flame, the precursor composition and concentration, as well as through the dispersion gas velocity and composition, [28].
Nanoparticles grow at temperatures greater than 2000 °C and follow four main stages, [21], [23]:

1. Precursor spray evaporation and decomposition until formation of metal vapour;

2. Nucleation as a result of supersaturation, in which a phase transition takes place;

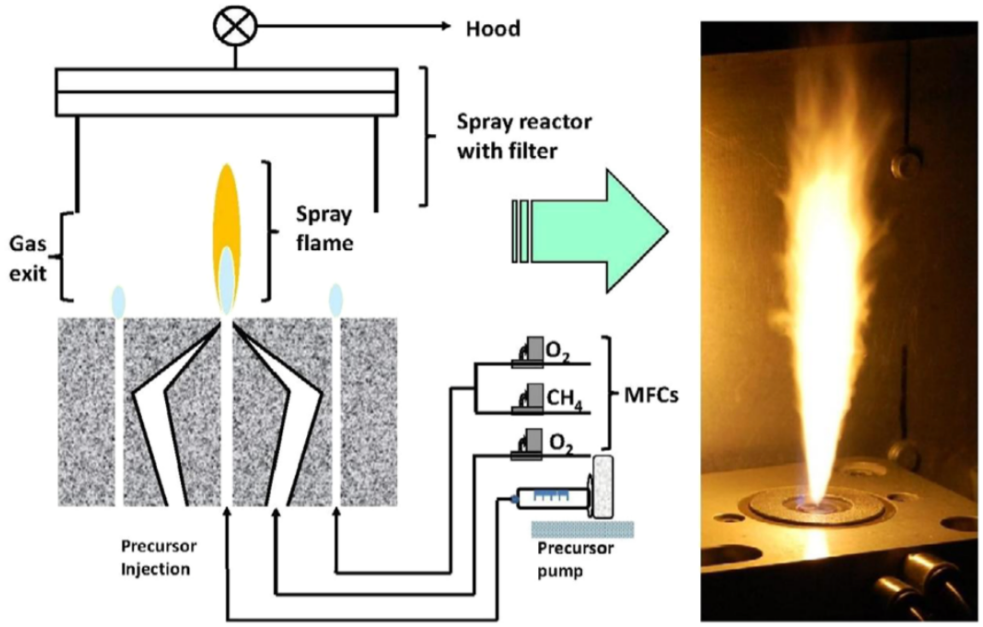

Figure 3.1. *Schematic of spray flame pyrolisis technology, [25]*

3. Surface growth by coagulation, coalescence and sintering;

4. Particles' aggregation (forming hard agglomerates by chemical bonds) and agglomeration (forming soft agglomerates by mainly physical bonds).

The nanoparticles are finally collected with a filter or deposited directly as porous film on the substrate placed above the flame. As a result, FSP-made nanoparticles are typically fully oxidized, crystalline and no other post-production treatments such as drying and calcination are strictly required. In addition, this method proved to be an effective one for the synthesis of nanosized and noble metal-modified TiO_2, yielding high porosity, high crystallinity, great anatase content and better noble metal dispersion, [29]. The schematic of this processes is easily shown in Figure 3.3, with the titanium oxide being nucleated and deposited on top of a glass substrate on which gold nanodiks were previously deposited through hole-colloidal lithography,

[10]. It is important to to take into account a new parameter known as height above burner (HAB) (Figure 3.2), which is the intersection distance between the nozzle and the substrate. Its optimization is very important in order to guarantee the complete particle formation.

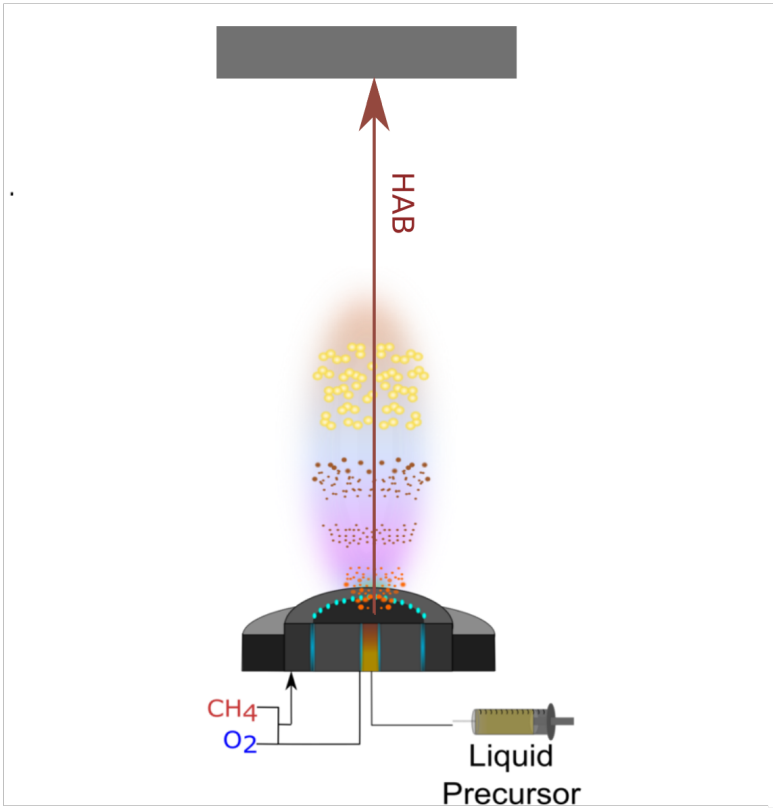

Figure 3.2. *Schematic of the SFSP with focus on the height above burner (HAB).*

In a previous work [10] the single flame sprays pyrolysis technique was used. In that case the TiO_2 precursor was dissolved in a liquid solvent (xylene) which fed the setup. During the residence time of the aerosol in the luminous region, several steps occurred, leading to aerosolizing of the precursor. Once the particle were formed they were then collected on the substrate -on which gold particles were already deposited- and self-assembled.

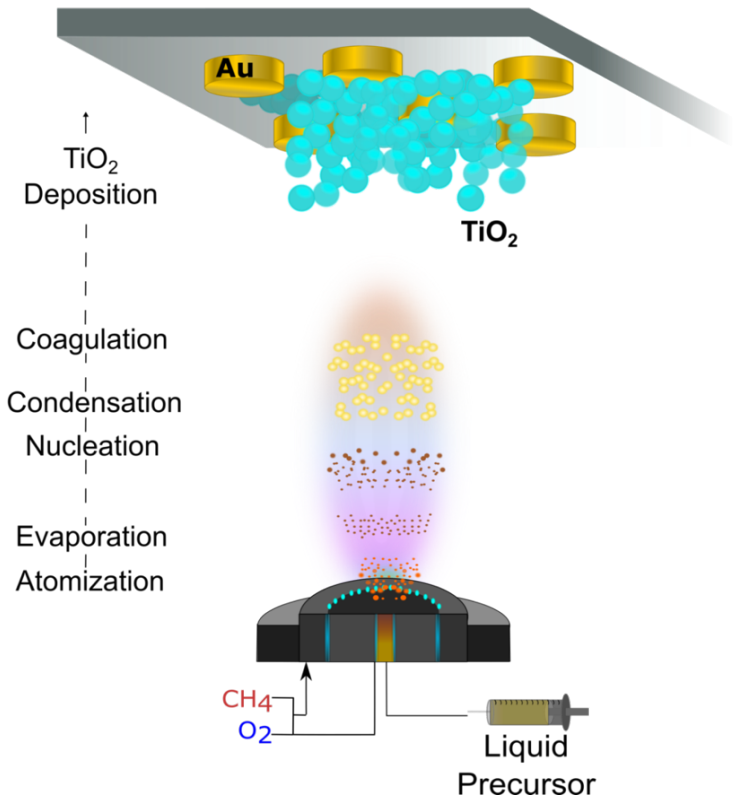

Figure 3.3. *Formation of TiO_2 nanoparticles (in light blue) through SFSP, [10]. Au nanodisks (in bright yellow) were previously deposited through litography techniques.*

3.2 Double Spray Flame Pyrolysis (DSFP)

The good performances of the single spray flame are now going to be improved with the use of the double spray flame pyrolysis where, in this case, the metal oxide precursors are combusted individually in two separate nozzles. This is particularly suitable when dealing with multicomponents. Figure 3.4 shows a schematic of the double flame setup that will be used in this project.
Having two individual flames instead of one allows a higher flexibility in tuning the resulting particles' properties, composition and size since preparation of both components can be individually controlled

in each flame during the synthesis, [24], [28]. As already told in the case of SFSP, nanoparticles' parameters can be controlled with the temperature profile of the flame and this is true for DSFP too. Here, however, the temperature profile depends mainly on the intersection distance of the flames and so it is adjustable with it. It is important to take it into account too because it will then influence the composition of the final synthesized material, [24]. The intersection distance, the height above burner (HAB), for both nozzles should have a length high enough to allow all the processes for particle formation as mentioned in the previous section.

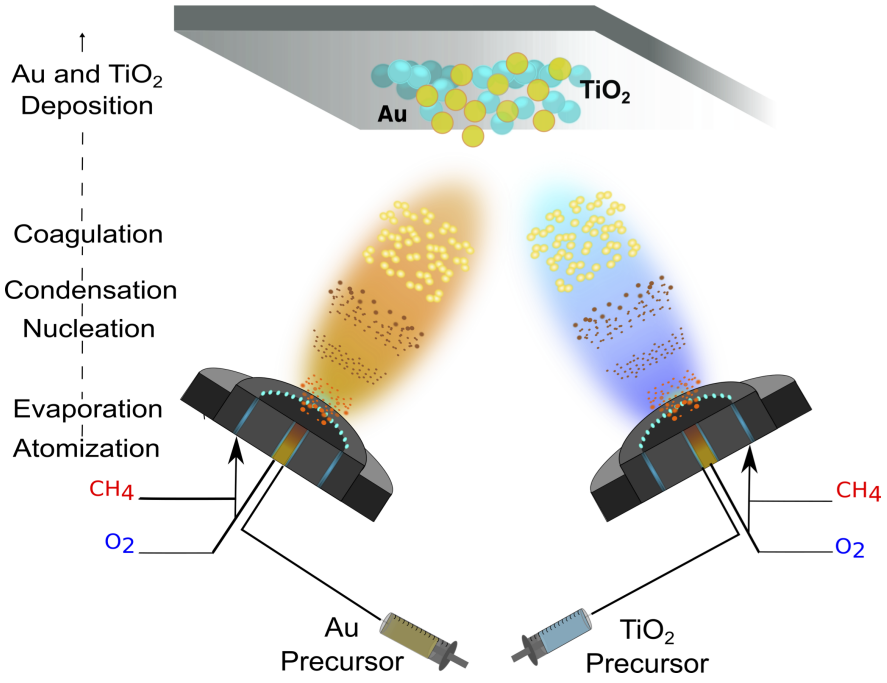

Figure 3.4. *Particle formation of both Au (in bright yellow) and TiO_2 (in light blue) nanoparticles through DFSP*

So DFSP offers the possibility to individually generate two different kind of nanoparticles (gold and titanium oxide in this specific work) in each flame and mixing them at a well-defined and adjustable flame

intersection distance. Therefore, one aim of this study was the investigation of flame configurations. The key factors which need to be considered in this case are the different particle formation steps during the synthesis: they are well known for a single flame, but have to be adapted to the double flame set up. When the flames intersect at small distances having both precursors still in the vapor phase a mixture of both oxides on the atomic scale is expected. Accordingly, formation of inactive spinels is likely, in analogy to the single flame approach.
An increase in intersection distance leads to the formation of individual oxide particles, which are well intermixed on particle scale. If the aerosol streams still provide enough energy at the intersection point, partial sintering of the individual oxide particles is possible.
An additional increase in intersection distance results then in a mixture on the agglomeration scale similar to the situation of the physical mixture of titanium nanoparticles with gold, but with much closer contact between the particles compared to physical mixing after collection of pure particles.
The main drawback is that precision is required otherwise the two compound not only do not mix in the desired amount, but also they may be not able to nucleate and thus cristallize.

3.3 Sample and setup preparation

Once the working principle of DFSP is clear, it is time to fabricate the samples to be finally tested. For this purpose 0.1 M TiO_2 precursor was prepared by adding 2.84 g of Titanium (IV) isopropoxide ($C_{12}H_{28}O_4Ti$) in 100 mL of Xylene (C_8H_{10}), while 0.01 M Au was syntesised by adding 0.34 g of Hydrogen tetrachloroaurate(III) ($HAuCl_4$) in 100 mL ethanol. In Figure 3.5 the final precursors are photographed. Please notice that gold shows its typical yellow colour

while titanium dioxide is mainly transparent. This means that the reactions ended successfully and ready for use in the flame process, whose preparation steps were mentioned in some previous works, [10], [28].

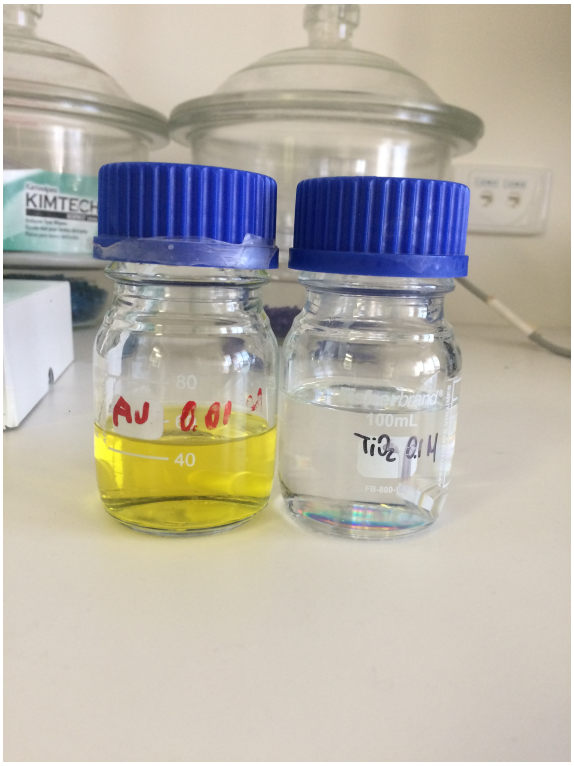

Figure 3.5. *Bottles containing 0.01M of Au precursor and 0.1M of TiO_2 precursor*

In the early stage of the process, due to the high flame temperature, an evaporation of the ethanol takes place, leading to a mixture of gold-salt particles. This is then dissociated to create Au^{3+} which is further reduced by thermal decomposition leading to the formation of pure Au particles. The residence time of the aerosol growth process has been found to be 30 ms; during this time, the Au aerosol starts a nucleation and condensation process. Sequential coagulation and aggregation of the Au nanoparticles happen in the flame region then these aggregates are collected on the cooled quartz substrate. The

same mechanism occurs for TiO_2 precursor too, as explained in [31].

The apparatus shown in Figure 3.6 is the one used for the fabrication of the samples. Each precursor solution is individually sprayed through two independent nozzles, but for both the working principle is the same. For each flame holder the liquid precursor solution is supplied at a constant rate of 5 mL/min and 3 mL/min for TiO_2 and Au respectively. In particular, precursors are injected through a syringe pump and dispersed into a fine spray (atomized) by a nozzle using 7 L/min O_2 at a constant pressure drop of 2 bars at the nozzle tip. In both cases spray is ignited by supporting premixed methane/oxygen flames ($CH_4 = 1.2$ L/min, $O_2 = 2$ L/min), resulting in a self-sustaining spray flame. Under these conditions, the particles are formed by reaction, nucleation, surface growth, coagulation and coalescence in the flame environment and collected on a cooled glass fiber filter. The intersection distance is adjusted properly both for the Au and the TiO_2, in particular the height above burner (HAB) of gold is set to 12 cm, while for titanium is set to 19 cm.

Four different samples were fabricated, differing from the deposition time: 45s, 90s, 135s, 180s. The main goal of next chapters will be a characterization for all of them together with a comparison and investigation of the performances. The final product is the one reported in Figure 3.7, with its characteristic pale-pink color due to the christallized gold nanoparticles surrounded by almost transparent christalline titanium oxide.

In the next chapter all the samples will be characterized, analyzed and tested for detection of selective organic volatile compounds.

Figure 3.6. *Double Flame Setup*

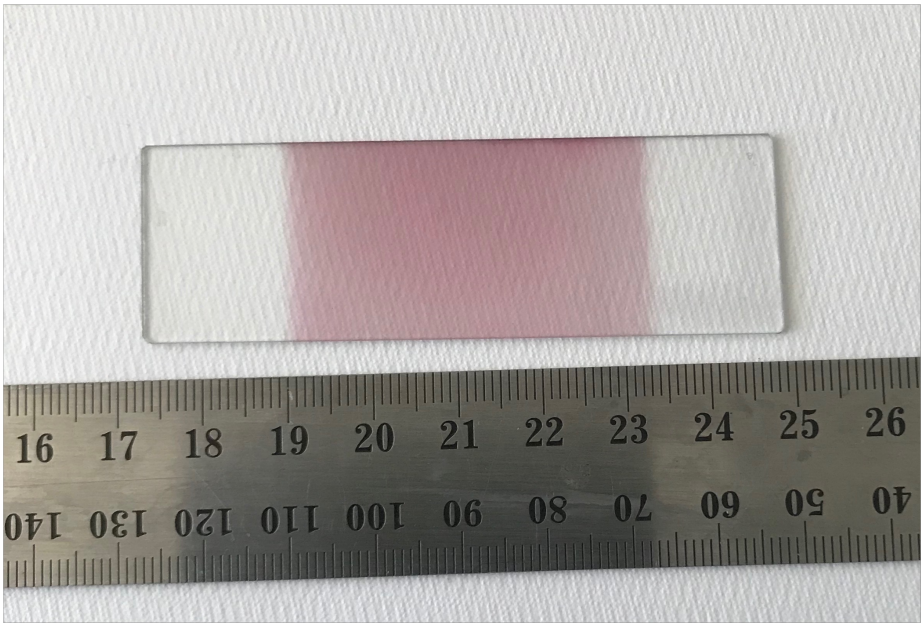

Figure 3.7. *One sample of Au and TiO_2 nanoparticles after a double flame spray pyrolysis process*

Chapter 4

Characterization and Simulations

Once that all the samples are finally fabricated, next step is the validation of sensitivity and performances. Before doing this, a characterization process is considered necessary to understand how the samples look. XRD patterns, SEM and TEM images proved to be fundamental for a quick evaluation of each sample's morphology. Finite Domain Time Domain (FDTD) simulations are carried too, taking into account how a flame-made sample looks. The main goal of these simulations is to compare the electric field enhancements -due to localised surface plasmon resonance- between a metamaterial and a metasurface. A neat difference between the two situations will be confirmed.

4.1 XRD

XRD (X-Ray Diffraction) analysis shows the intensity of X-Ray patterns at different angles by a sample. This kind of analysis is able to define the crystalline phases of an atom, which means that through XRD the atomic arrangement within the crystal can be detected. The instrument is made of an X-Ray tube and a detector, which moves of 2θ describing a circle. At the same time, to keep the X-ray beam properly focused, the X-ray beam rotates too. Since the X-ray diffraction pattern is different for each phase, the final plot will consequently

be a superposition of the diffraction patterns of each individual phase. Each diffraction peak is associated to planes of atoms that can be identified with Miller indices (hkl): they define the reciprocal of the axial intercepts and represent the orientation of the crystallographic plane. Another important parameter to compute is the vector extending from the origin to the plane (hkl) and is normal to (hkl), d_{hkl}: it represents the distance between parallel planes of atoms in the family (hkl) and depends on size and shape of the unit cell. This vector is used in Bragg's law (Equation 4.1) to determine where diffraction peaks will be observed:

$$d_{hkl} = \frac{\lambda}{2sin(\theta)} \tag{4.1}$$

with λ the operating wavelength of the XRD instrument. What d_{hkl} does not reveal, however, is the size of the nanoparticle itself. To overcome this problem one can compute the Debye-Scherrer equation (Equation 4.2), that relates the size of the particle with the angle and d_{hkl}:

$$B(2\theta) = \frac{K\lambda}{(FWHM)cos(\theta)} \tag{4.2}$$

with K defined as Scherrer constant, which depends on many factors such as the shape of the crystal and the size distribution; FWHM is the full width at half maximum expressed in radians, while $cos(\theta)$ is expressed in degrees. In this work $K = 0.9$ and the XRD instrument is equipped with Cu-Kα radiation of average wavelength $\lambda = 1.54059$ Å.

Figure 4.1 shows the XRD spectra of each sample. The diffractograms were compared with literature data for phase recognition, [29], [30]. Those peaks related to gold are easily recognizable, and their intensity increases as the deposition time increases, suggesting that the quantity of gold in the sample increases with it.
Concerning TiO_2 peaks, they are located in the range between 20° and 35° and are associated to highly anatase crystal peaks. Please notice that, generally speaking, there is no indication of any crystal phase change: this means that even by varying the deposition time each sample keeps the same chrystallographic structure. This is perfectly coherent with flame spray as aerosol synthesis process, because the very high temperatures will allow an instant particle formation together with a high crystallinity and so low crystal defects.

Thanks to Scherrer equation, particle sizes of both gold and titanium oxide have been calculated for every sample, as reported below in Table 4.1, from which it is possible to notice that gold has a particle size between 10 nm and 22 nm, while for titanium oxide it changes from approximately 7 nm in the 45s sample to 9.5 nm in the 180s sample.

Sample	Deposition Time [s]	d_{Au} [nm]	d_{TiO_2} [nm]
1	45s	12.3307	7.7593
2	90s	19.1127	8.8900
3	135s	19.1161	9.3910
4	180s	21.7030	9.5114

Table 4.1. Particle sizes of Au and TiO_2 nanoparticles in nm according to the XRD pattern

Knowing that samples will be excited by an incident light having wavelengths in the range between 400 and 800 nm and given the definition of nanoparticles, Table 4.1 gives prove that flame-made Au and TiO_2 are effectively *nanoparticle* so theoretical discussion in Chapter

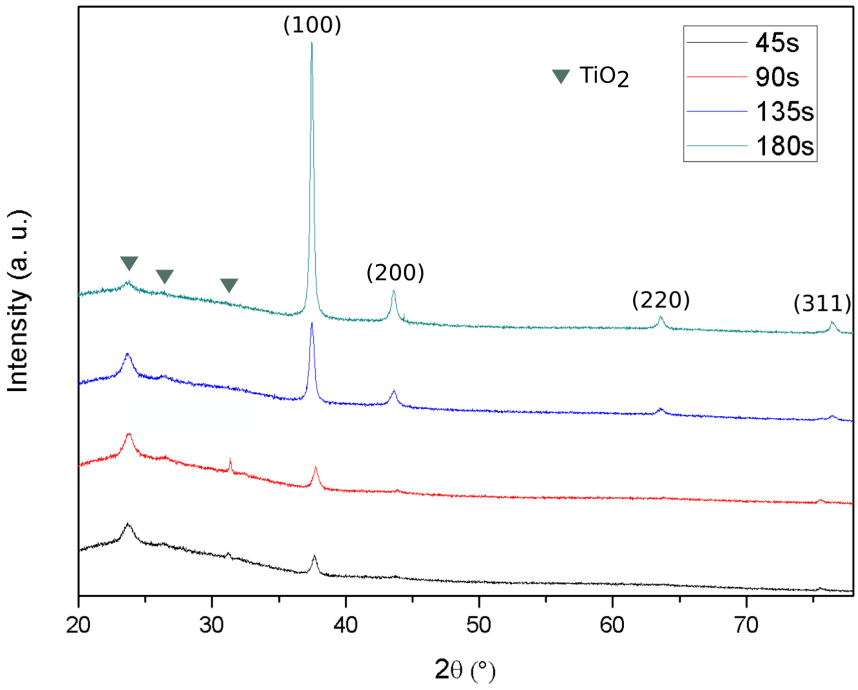

Figure 4.1. *XRD patterns of the four samples: 45s, 90s, 135s, 180s. Au diffraction peaks are marked with their crystallographic orientation, while TiO_2 peaks are marked with triangles*

2 are valid.

4.2 SEM

Scan Electron Microscopy (SEM) exploits electron beams instead of light to observe samples at the nanoscale. The electron beam is generated by a filament, the electrons follow a certain pattern in which they are accelerated and collimated to a set of electromagnetic lenses and finally they are defleted by an objective lens. This procedure is essential for scanning the sample.

Figure 4.2 and Figure 4.3 are the SEM images of a sample obtained after five minutes of deposition, as representative for all the other samples. The high porosity of the titanium clusters is very evident (Figure 4.2), as well as the small dots representing the gold nanoparticles trapped inside it (Figure 4.3).

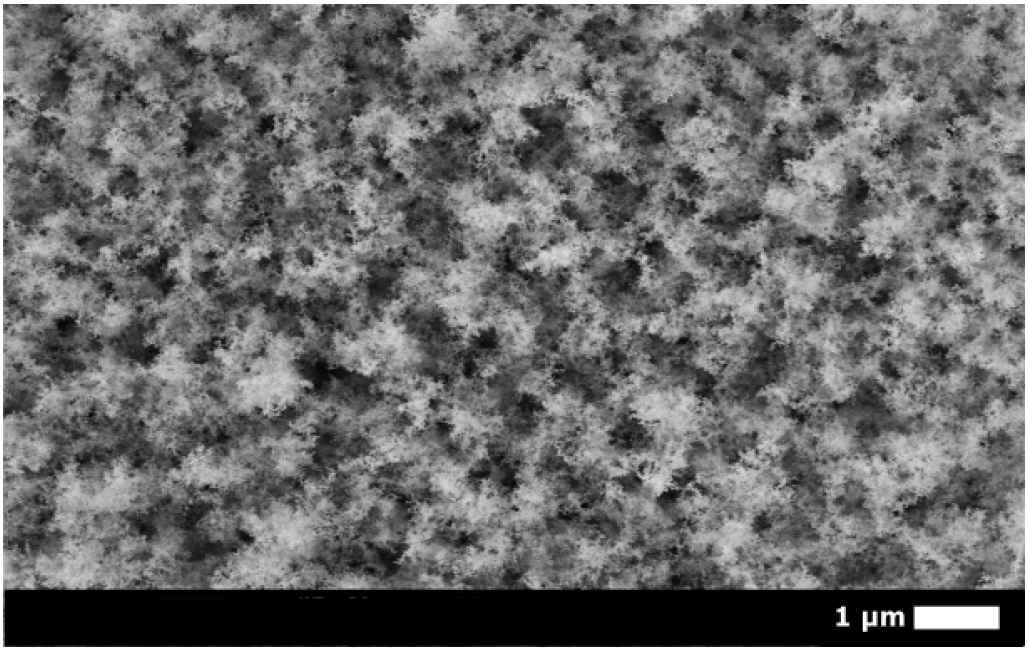

Figure 4.2. *SEM image of a dielectric film made of TiO_2*

For a porous film two main effects can take place by increasing thickness: an increase of the total available surface for interaction with the gas that has to be detected, but at the same time a decrease in the gas concentration at the bottom of the film, [14]. A good compromise for choosing the film thickness must be found, as it may affect the final results: an increase of it may improve the gas reception sites, [14], but with too thick films the sensor response is likely to be decreased due to the combustion of the gas itself in the upper layer of the film. Thus, an optimization of the film thickness is necessary to maximize the sensor performance.

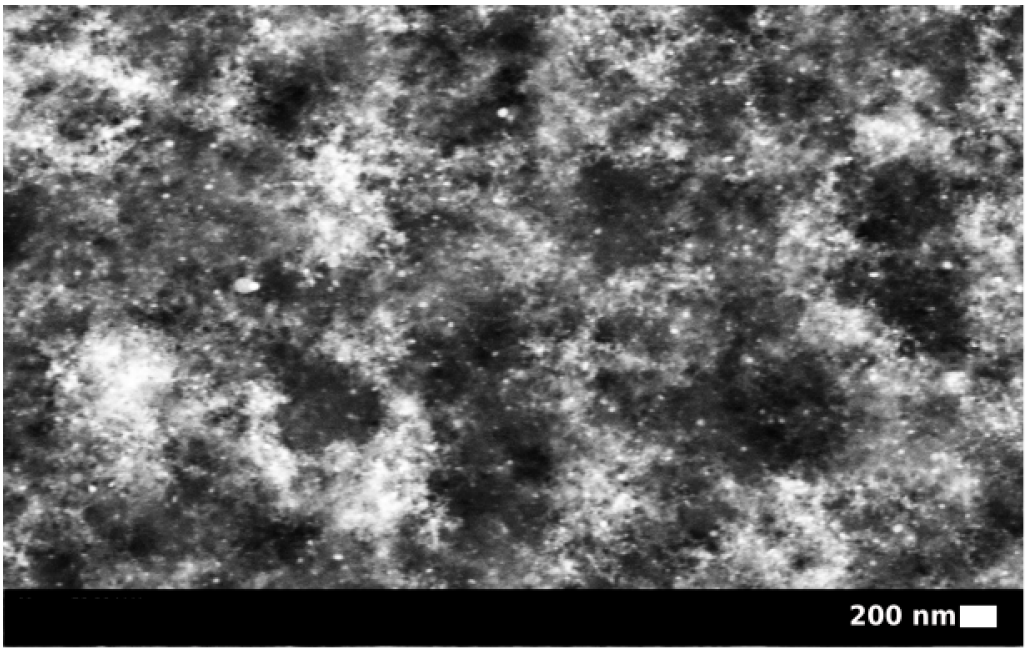

Figure 4.3. *Top view SEM image of the trapped gold nanoparticles*

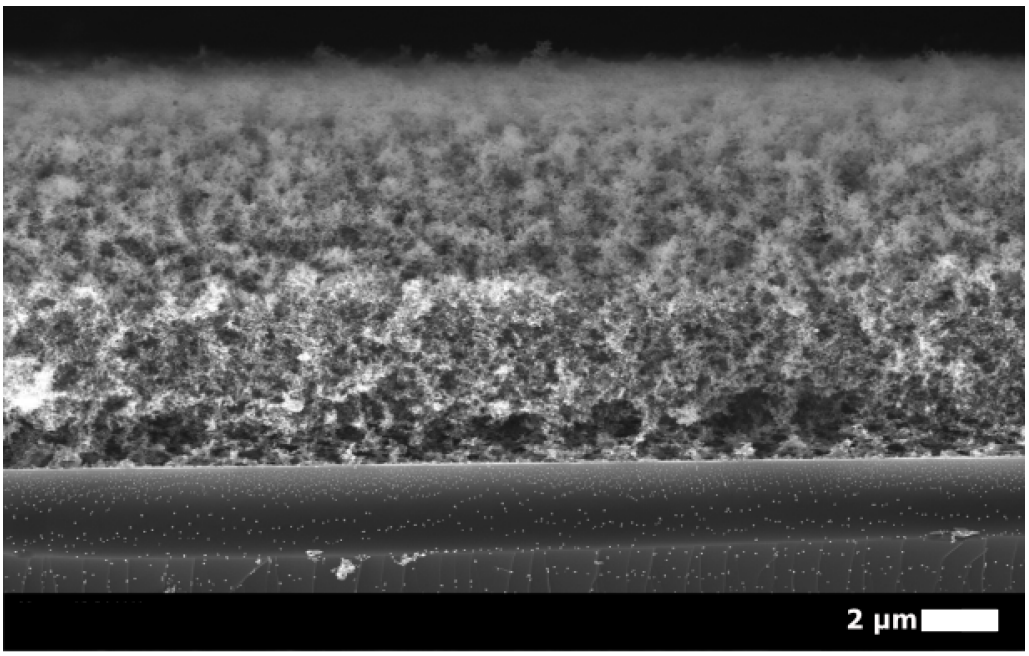

Figure 4.4. *SEM cross-section image of the trapped gold nanoparticles*

At first glance, from the SEM images (Figure 4.2 and Figure 4.3) it turns out that the numerical density (which is the number of gold nanoparticles per volume) is around 10 spheres in a 200x200x200 nm^3 volume, which is very close to the predictions in Section 2.3.
Figure 4.4 shows the cross-section SEM image of one sample: there are some tiny white dots representing the gold nanoparticles (visigle in Figure 4.3) that at first, in absence of the scaffold in titanium, deposit on the substrate, with an ultra porous structure representing the titanium scaffold. According to the cross section SEM images (Figure 4.4), thicknesses for each sample are computed and they increase almost linearly as the deposition time increases: 1.45 μm for 45s, 2.85 μm for 90s, 4.40 μm for 135s and 6.10 μm for 180s. This is clearly reported in Table 4.2 and from now on each sample will be identified by the thickness.

Sample	Deposition Time [s]	Thickness [μm]
1	45s	1.45
2	90s	2.85
3	135s	4.40
4	180s	6.10

Table 4.2. Particle sizes of Au and TiO_2 nanoparticles in nm

By varying the thickness one should expect to obtain better performances and consequently better shifts, but this implication is not completely true: as it will be proved in the next sections, an increase in the growth will lead to a great electric field enhancement, but worse sensing results.

4.3 TEM

When a sample is inserted in a TEM (transmission electron microscopy) microscope, only a small amount of the incident electron beam hits

the sample itself and only those that are not dispersed contribute to the formation of the final TEM image.

Figures 4.5 and 4.6 show the TEM image of a small piece of one sample. From Figure 4.6, in particular, the wrapping of titanium around the gold nanoisland is evident: this means that an aerosol flame spray synthesis of both materials at the same time not only produces very christalline structures, but they also agglomerate and frame one another. These images also confirm the role that TiO_2 employs as a scaffold for gold nanoparticles. In addition, from these images the particle size of TiO_2 can be computed and for all the samples this turns out to be around 10 nm, which is coherent with the data collected in Table 4.1

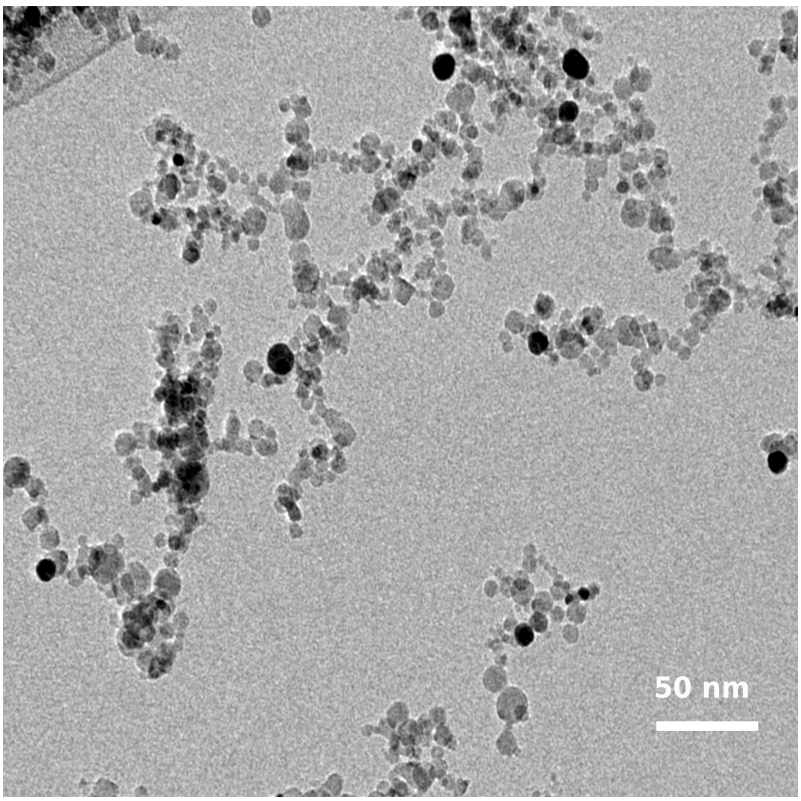

Figure 4.5. *TEM image of a Au (in black)-TiO_2 (in light gray) cluster*

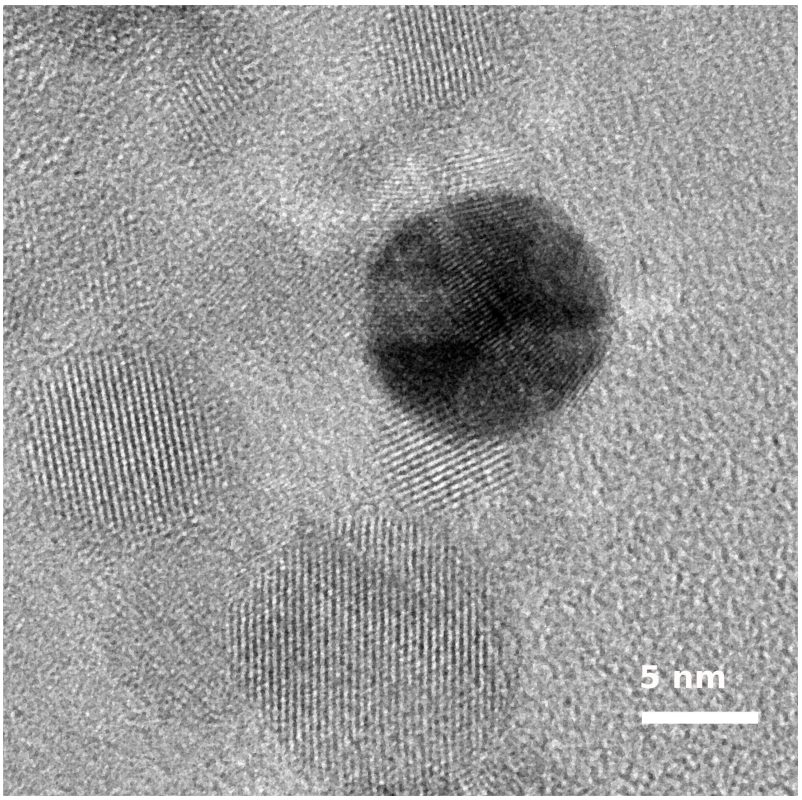

Figure 4.6. *TEM image of Au nanoparticle (in black) surrounded by TiO_2 nanoparticles (in white/gray)*

4.4 Simulations

Electrodynamic simulations based on Finite-Difference Time-Domain (FDTD) is performed with Lumerical FDTD software, this time knowing how the dimensions and distribution of the samples. In this way a more crytical analysis can be carried out.
To do so, a box of dimensions of 100x100x450 nm^3 is created and and filled both with TiO_2 and Au spheres: each sphere is generated by a Matlab code running the real distribution of particles when distributed om the substrate through flame spray synthesis. Au dimensions are chosen similar to the experimental results of the best response sample, which turns out to be around 30 nm (4.40 μm sample). Particle size

of TiO_2 is fixed to 10 nm. The same process is done for assembling a bilayer too.

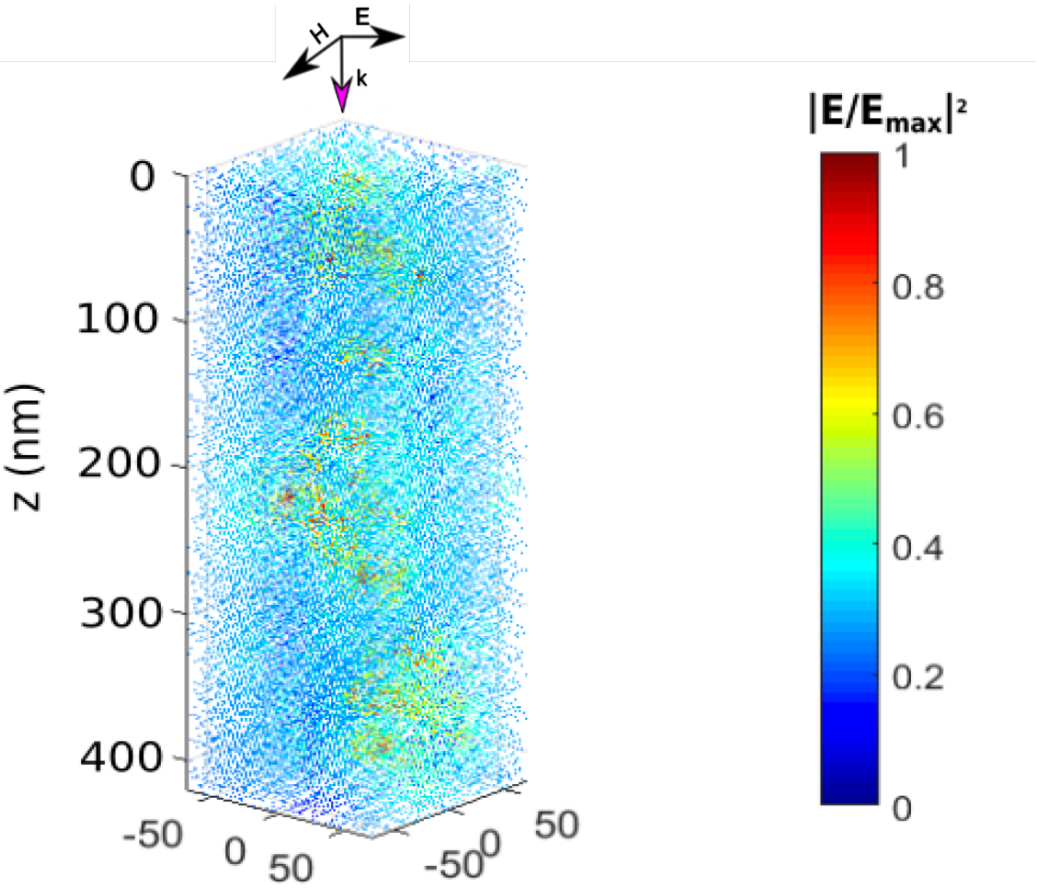

Figure 4.7. *Normalized vectorial electric field of a 3D plasmonic resonant metamaterial*

Figures 4.7 and 4.8 represent the vectorial normalized electric field elaborated with Matlab both of the 3D architecture and bilayer, respectively. From these preliminary results, it seems that in the 3D metamaterial the electric field is improved in the whole structure thanks to the golden nanoparticles sustained by titanium, randomly distributed in the structure and coupling among each other. In the

case of bilayer, instead, there is a big enhancement on top of the structure (where the substrate is and, thus, the gold spheres are supposed to be located) and then a huge decrease as soon as the distance from the gold nanodisks increases.

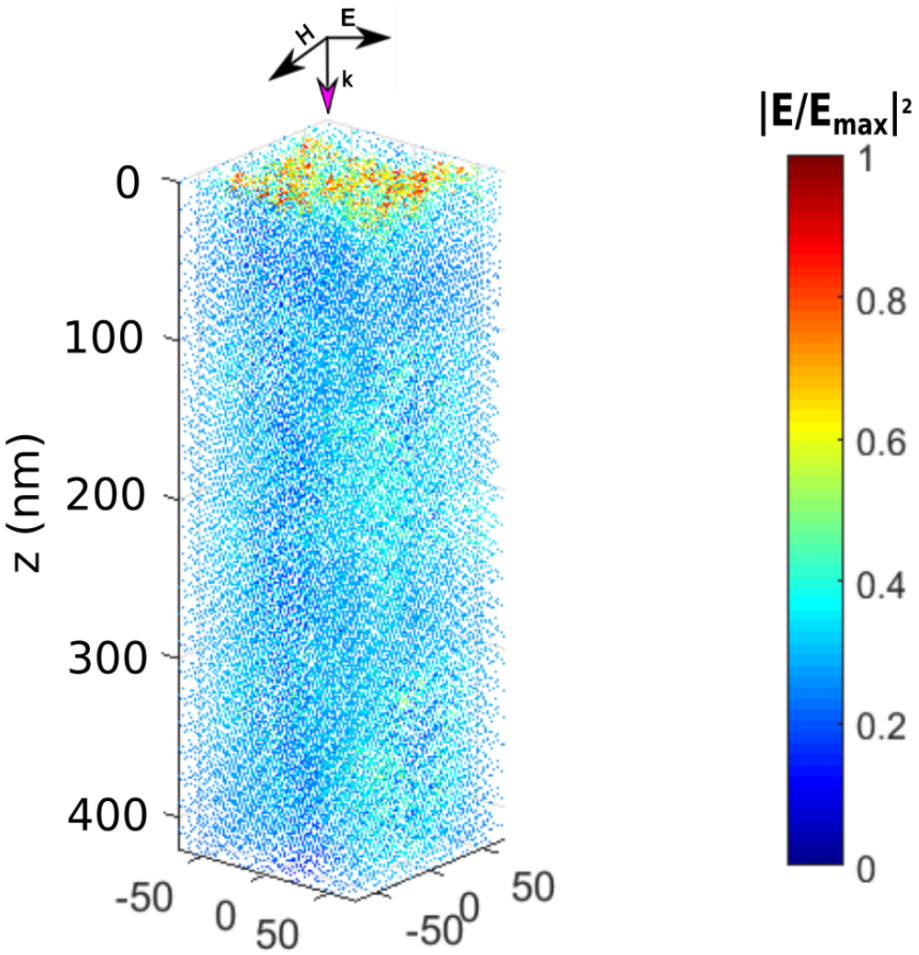

Figure 4.8. *Normalized vectorial electric field of a plasmonic bilayer*

To further prove the validity of such preliminary results, for both structures different slides are taken and the enhancement is analysed and compared. Figure 4.9 shows the behavior of the electric field in the case of a metamaterial: one should notice that in this case of 3D

structures gold nanoparticles interact among themselves, in particular they start to couple the electric field and electron clouds. This leads to a huge improvement of the electric field itself, as it is possible to see.

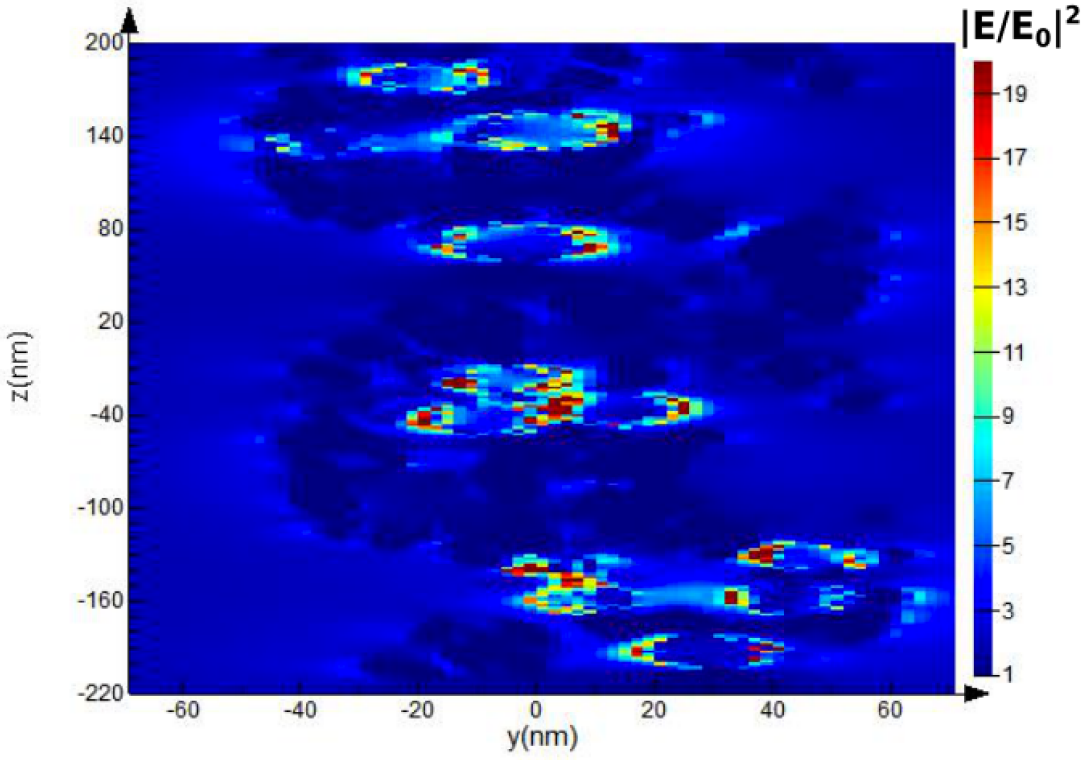

Figure 4.9. *Normalized Electric field enhancement of a 3D plasmonic resonant metamaterial*

In the case of the bilayer (Figure 4.10), none of the aforementioned phenomena take place, indeed it shows a quite high electric field just at the beginning because the gold is placed only on the substrate, and then it goes flat decreasing rapidly. This suggests a very local and limited enhancement in the case of the bilayer, while on the other hand a big improvement in the case of the metamaterial. From these results some more accurated considerations can be carried out.

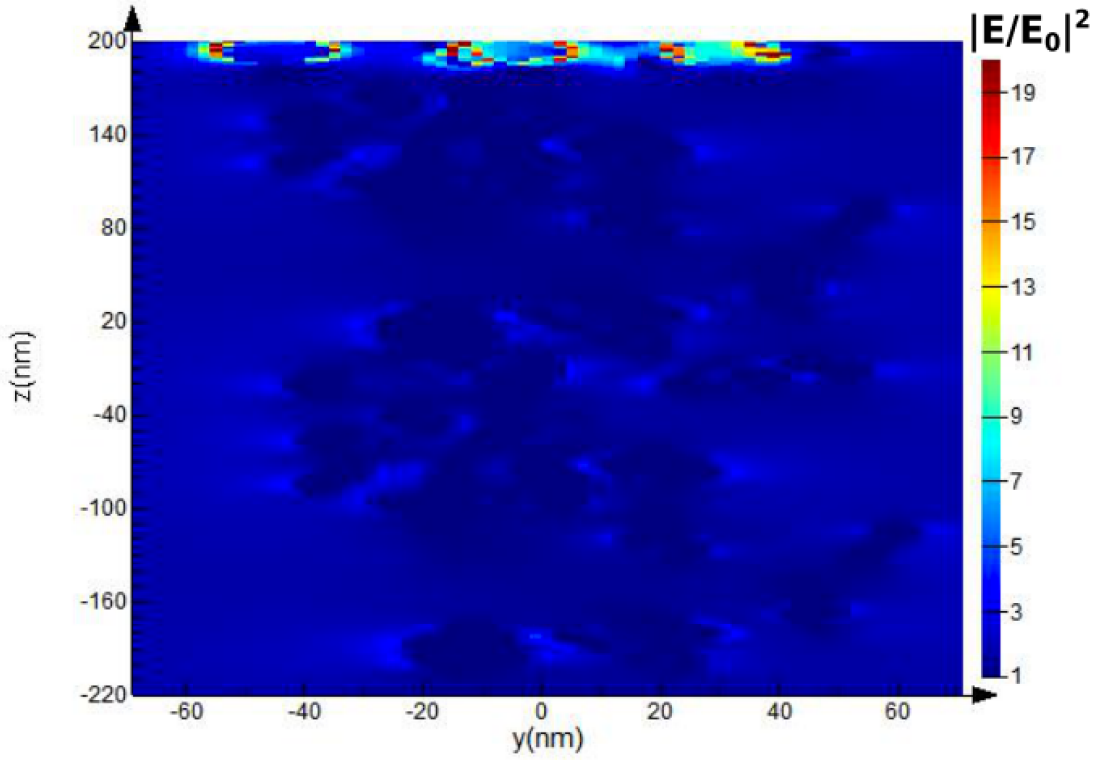

Figure 4.10. *Normalized Electric field enhancement of a plasmonic bilayer*

A more concrete quantification of this sensational behavior can be provided by showing the *neat* enhancement of the electric field which is, in other words, how the electric field of the gold spheres given the presence of titanium oxide behaves both in the case of a frozen island (a christalline sphere "immersed" in titanium oxide) and of a bilayer. This result is carried out by computing the potential energy of both models: taken the electric field this is integrated by the volume of the structure. So final plots (Figures 4.11 and 4.12) will show the potential energy of the cluster as a function of the wavelength at fixed volumes (obtained by changing the dimension along z axis only).

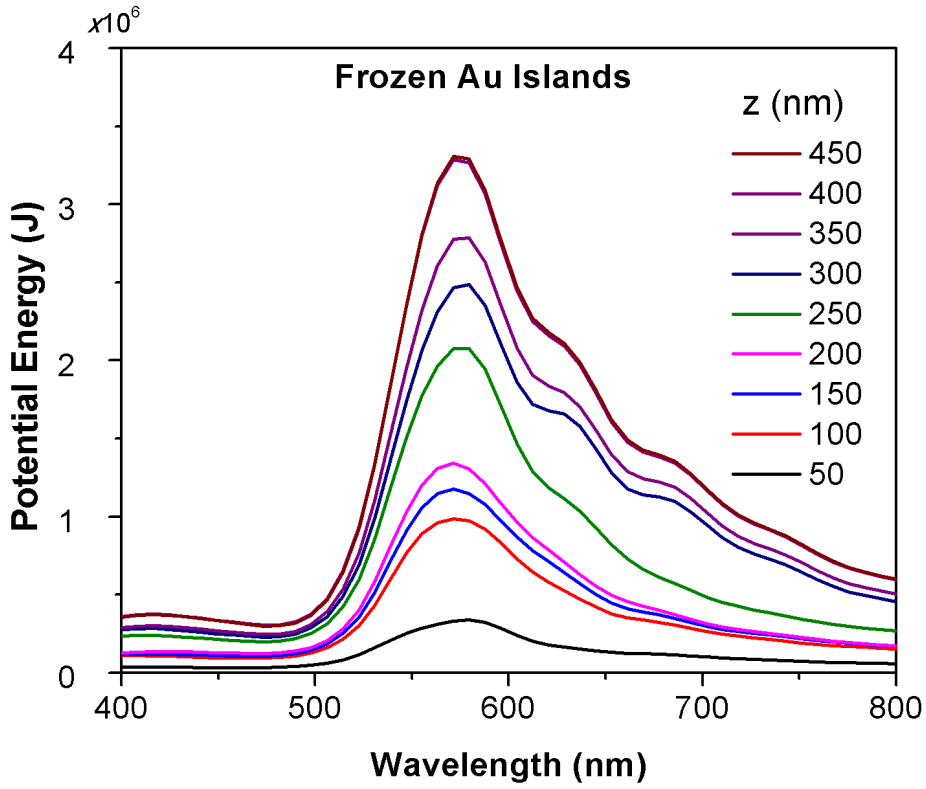

Figure 4.11. *Potential Energy, expressed in Joule, of the 3D metamaterial as a function of the wavelength*

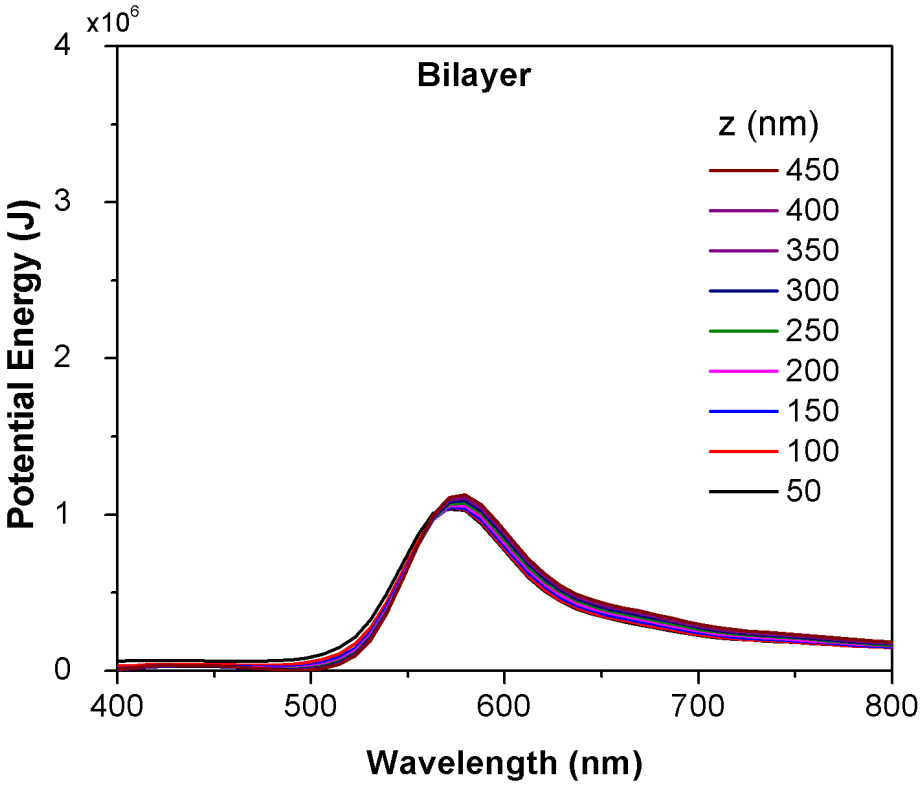

Figure 4.12. *Potential Energy, expressed in Joule, of the plasmonic bilayer as a function of the wavelength*

It is clear that the frozen gold nanoislands (Figure 4.11)show an enormously increasing potential energy as the thickness of the titanium increases, with a sharp peak in the visible range, where plasmonic effect should take place. This is a huge improvement with respect to the bilayer (Figure 4.12) which shows no relevant improvements at all. Quantitatively speaking there is almost a three times enhancement of the plasmonic effect in a metamaterial rather than in a metasurface.

Chapter 5

Sensing Results

In the previous chapter, thanks to characterizations and simulations, one can have an idea on how each sample looks and how should they behave. This chapter will illustrate the optical gas sensing of the metasurfaces at room temperature with different gases (i. e. ethanol, toluene, acetone) at different percentages. The main goal is to reach lower limit of detections and confident about the results coming from the simulations in Section 4.4 one should expect good performances. Specifically each sample is able to detect up to 1 vol% of any of the tested analyte with a different shift and react very well to a variation of the external environment.
In addition it could be useful to find out the overall selectivity and stability of each sample, that together with the sensitivity (already discussed in Chapter 2) are three important data for a sensor of any kind. So these are two useful parameters to evaluate if, generally speaking, a sensor can provide a good performance: selectivity is the capability of a sensor to discern among different species of analyte, while stability is related to how the sensor keeps the same response even after a huge amount of time.

5.1 Setup Preparation

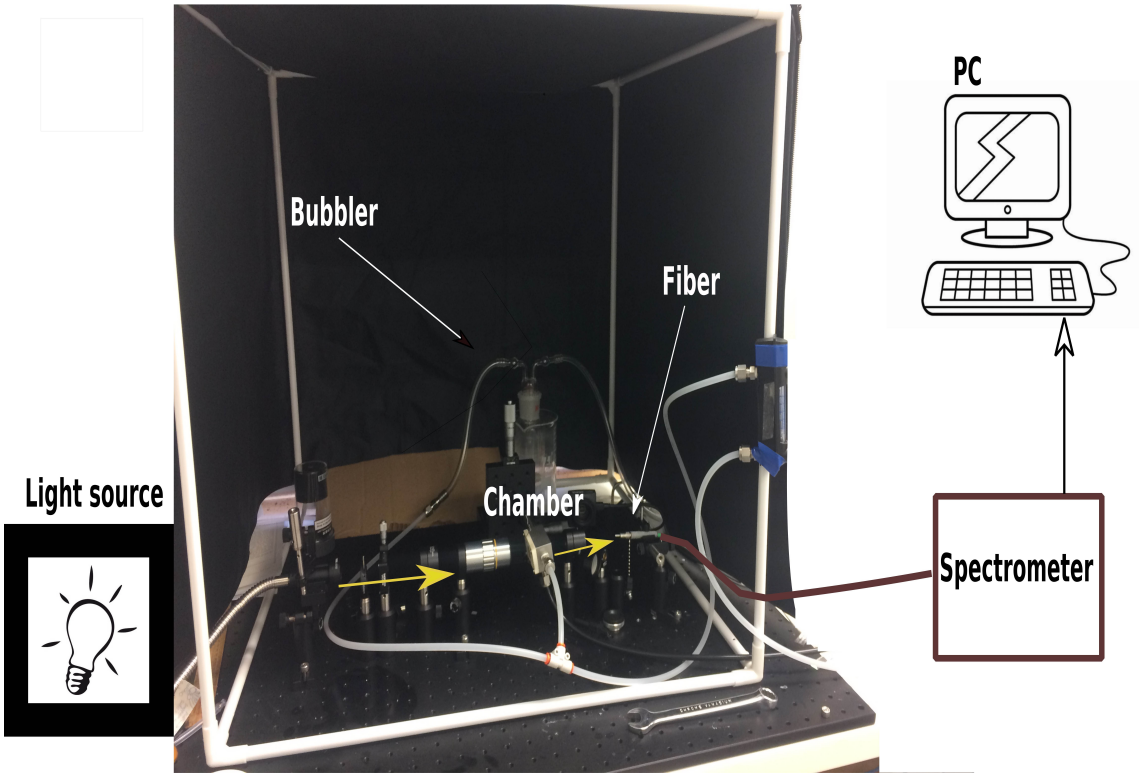

Figure 5.1. *Sensor setup*

Figure 5.1 shows the optical setup prepared for testing the extinction spectroscopy of LSPR active substrates. It consists of an halogen lamp sending, through a system of collimating lenses, light beams to a chamber containing the sample. The output is collected into a fiber connected to a spectrometer. The spectrometer is connected to a PC via USB port. This PC acquires and analyzes data continuously. After all samples are collected, the peaks are found thanks to the algorithm in [32].
Gases are injected in the chamber through some tubes, and two valves control gases inlet and outlet. One valve controls the simulated air

while the other was responsible for injecting pure air and the gas, thus they can not be opened or closed at the same time. Before entering the tubs leading to the chamber, simulated air (here a mixture of nitrogen and oxygen) is mixed with the gas through a bubbler. The amount of air to be injected is set up manually (N_2 = 0.8 ml/min, O_2 = 0.2 ml/min), while the gas flow rate is set up thanks to a flow bar.

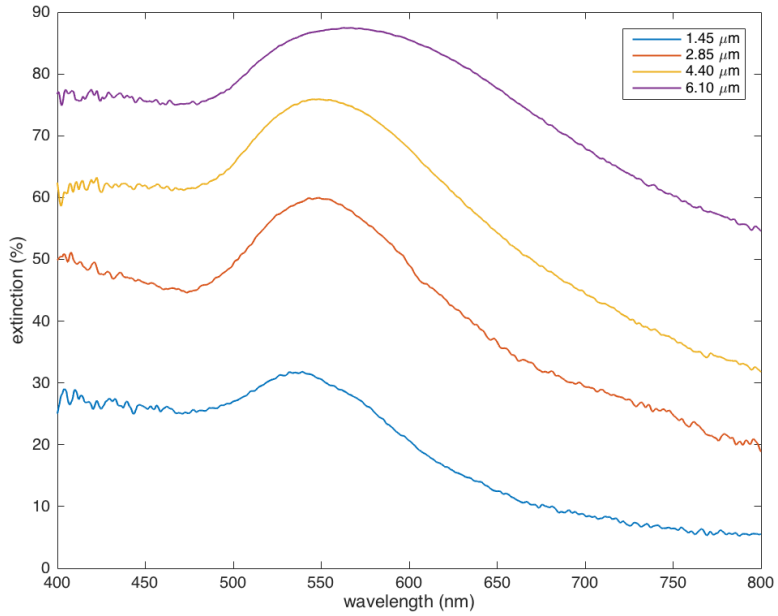

Figure 5.2. *Extinction cross section of the four samples in air*

Once the sample is in the chamber it is firstly exposed to air. Figure 5.2 represents the extinction cross section of each sample in simulated air. These profiles could be considered as "offsets" for each sample, because each one should be able to come back to this shape if some gases are injected and then removed from the chamber.
Figure 5.3 shows a visible plasmonic shift of the best sample, which is perfectly in line with the theory (Figure 2.6 in Chapter 2): not only the enhancement of the plasmonic peak along the wavelength axis is

very clear, but also a higher increase in terms of intensity in the extinction cross section function is visible. This result is very challenging as it represents a big step forward in LSPR particles sensing, most of all if compared with the performances of a bilayered architecture made of the same materials, [10].

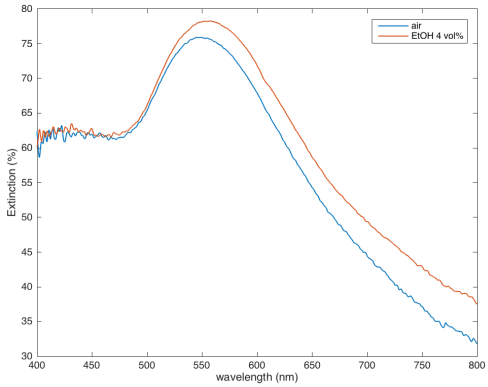

Figure 5.3. *Dynamic response of the resonance peak position of the best sample to different cycles of air/EtOH at room temperature*

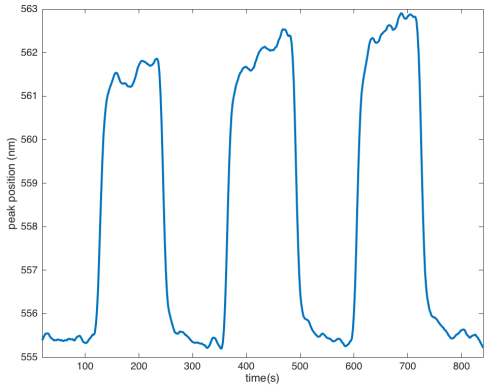

Figure 5.4. *Dynamic response of the resonance peak position of the best metamaterial sample to different cycles of air and 4 vol % toluene at room temperature*

Figure 5.4 represents the dynamic response of the best sample when exposed to a 4 vol % concentration of toluene. This picture wants to point out that the frozen islands are very sensitive as they are capable to change their extinction peak in less than a second, and also it is quite stable since the plasmonic shift is always around 7.2 nm even after some cycles.

In the next sections the samples will be tested under different cycles of air and three different gases, which are ethanol, toluene and acetone, as they result as possible biomarker for important diseases such as lung cancer and diabetes. It will be interesting to see how low is the concentration of gas each sample can detect.

5.2 Ethanol (EtOH)

Ethanol is the standard test volatile compound, but it is considered a potential biomarker for diseases related to alcohol and cigarette consumption, [17]. Its formula is CH_3CH_2OH.
The interaction of EtOH with the TiO_2 at low temperatures are based on the adsorption of EtOH through a hydroxyl group (O-H): the adsorption takes place thanks to the O-H bond cleavage leading to the formation of CH_3CH_2O and hydrogen H that reacts with the active oxygen on the TiO_2 surface, [10].
In all cases there is a fast response dynamics and a good stability, meaning that all samples not only react very well to a change in the external environment, but also it is able to restore itself back when it comes to the initial situation. This fast response is due to the high porosity, which enables a reversible adsorption of the gas molecules in the whole fractal film, [10].
An interesting results may be related to the fact that there is not a linear increase of the plasmonic shift with respect to the thickness: indeed, there is an improvement as much as 4.40 μm thickness is reached (Figure 5.7), then the shift decreases. This is clear in Table 5.1. The reason is probably due to the thickness itself, because if this parameter increases too much, then the gas is not able to penetrate that deep into the cluster and so not all the gold nanosphere will resonate and contribute to the electric field enhancement.
In any case, the results are very challenging for all the samples, as all of them are able to detect ethanol at concentration up to 1 vol% at room temperature (assumed to be around 22 °C). For this reason extra tests are performed with a decreasing concentration of gas.

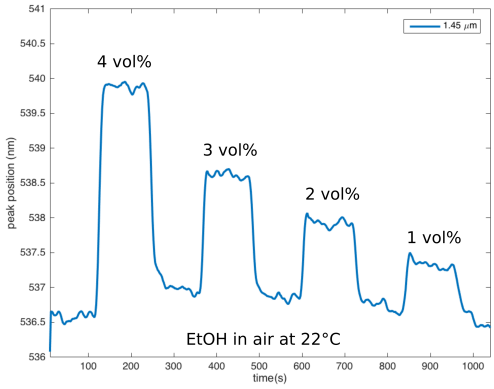

Figure 5.5. *Dynamic response of the resonance peak position of sample 1.45 μm to different cycles of air/EtOH at room temperature*

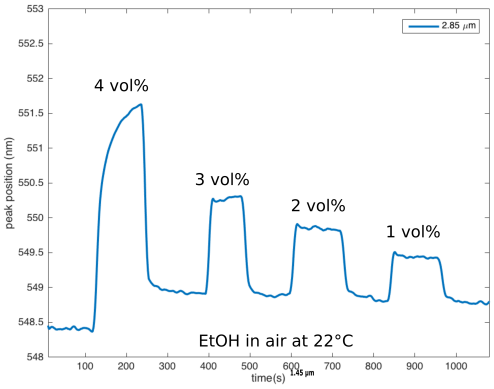

Figure 5.6. *Dynamic response of the resonance peak position of sample 2.85 μm to different cycles of air/EtOH at room temperature*

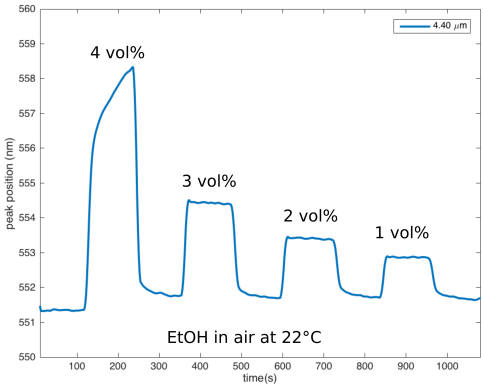

Figure 5.7. *Dynamic response of the resonance peak position of sample 4.40 μm to different cycles of air/EtOH at room temperature*

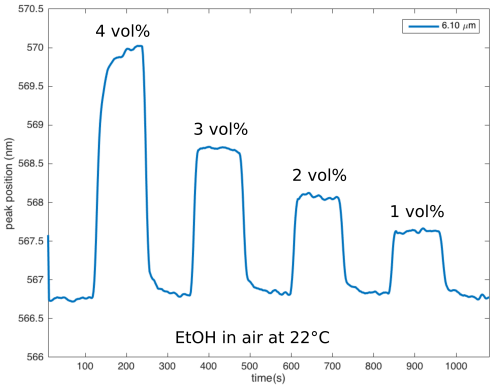

Figure 5.8. *Dynamic response of the resonance peak position of sample 6.10 μm to different cycles of air/EtOH at room temperature*

Thickness [μm]	Concentration [vol %]	$\Delta\lambda_p$ [nm]
1.45	4	3.00
”	3	1.60
”	2	1.00
”	1	0.70
2.85	4	3.10
”	3	1.30
”	2	1.00
”	1	0.85
4.40	4	7.00
”	3	2.80
”	2	1.80
”	1	1.20
6.10	4	3.30
”	3	2.0
”	2	1.30
”	1	0.70

Table 5.1. Dynamic response of each sample to different >1 vol % concentrations of ethanol

5.2.1 Low limit of detection

In this bunch of new tests the real efficiency of each sample comes out (explicit results in Table 5.2), because it seems that sample 1.45 μm is not performant at all when exposed to very small concentration since not only the lineshape is very wavy (Figure 5.9), but also it is not able to restore back to equilibrium for concentrations less than 0.1 vol%. Almost the same comment can be told for sample 6.10 μm (Figure 5.12), even if in a less dramatic way: this sample is not able to give a neat response upon 0.01 vol % but at the same time is not noisy as sample 1.45 μm. The best response is given by sample $4.40\mu m$ (Figure 5.11), which is able to keep its responsiveness and stability even at concentration as low as 0.01 vol% which corresponds to 100ppm (parts per million) : it is almost one order of magnitude less with respect to common bilayered sensors.

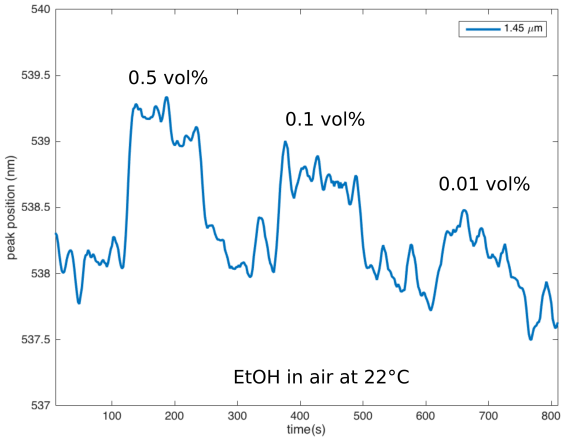

Figure 5.9. *Low limit of detection of sample 1.45 μm exposed to EtOH at room temperature*

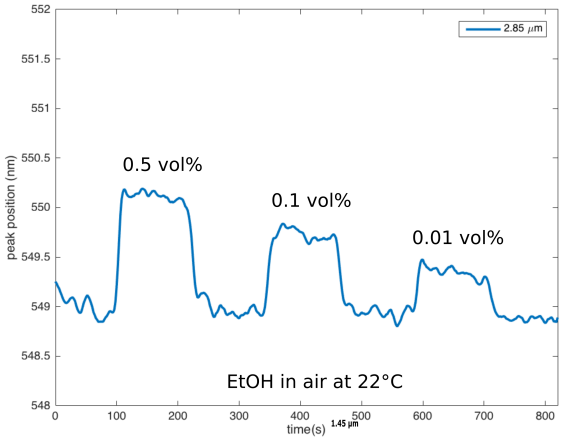

Figure 5.10. *Low limit of detection of sample 2.85 μm exposed to EtOH at room temperature*

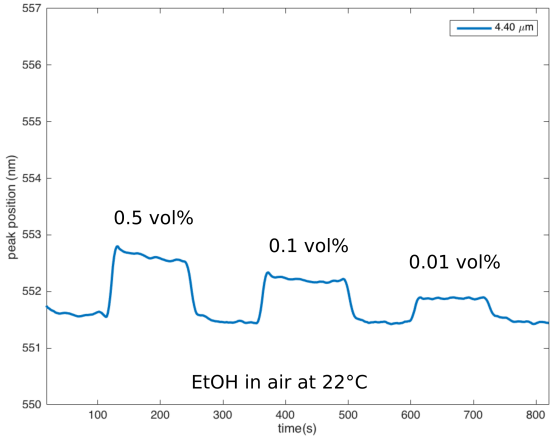

Figure 5.11. *Low limit of detection of sample 4.40 μm exposed to EtOH at room temperature*

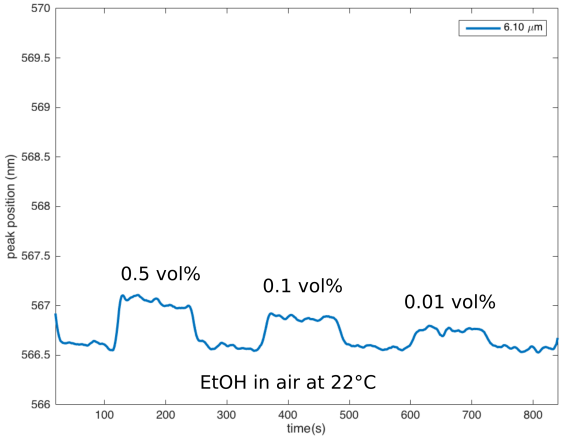

Figure 5.12. *Low limit of detection of sample 6.10 μm exposed to EtOH at room temperature*

Thickness [μm]	Concentration [vol %]	$\Delta\lambda_p$ [nm]
1.45	0.5	0.60
”	0.1	0.40
”	0.01	0.10
2.85	0.5	0.80
”	0.1	0.70
”	0.01	0.50
4.40	0.5	1.0
”	0.1	0.90
”	0.01	0.40
6.10	0.5	0.60
”	0.1	0.40
”	0.01	0.20

Table 5.2. Dynamic response of each sample to different very low concentrations of ethanol

5.3 Toluene

Toluene is an aromatic volatile hydrocarbon, with formula C_7H_8. This one is a biomarker related to diseases derived from alcohol and cigarette consumption too.
Depending on the orientation of the benzoic ring in toluene, the absorption of this gas to TiO_2 can happen in different ways: if the ring is orthogonal to the TiO_2 surface the methyl group dissociates and interacts with oxygen, but if the ring is planar to the surface, it will likely bind through the hydroxyl groups. The condensation increases the local refractive index near the surface of TiO_2 by increasing the LSPR response and device sensitivity, [10].
Same comments as in the case of ethanol are valid (results reported in Table 5.3): there is a neat enhancement when the thickness of the TiO_2 reaches 4.40 μm, then the performances decrease. Also with toluene all samples are reactive, stable, and capable to detect concentrations up to 1 vol%. They all respond very well at very low concentration (up to 1 vol%), but the one that is able to give the best performance

is still the 4.40 μm (Figures 5.15 and 5.19).

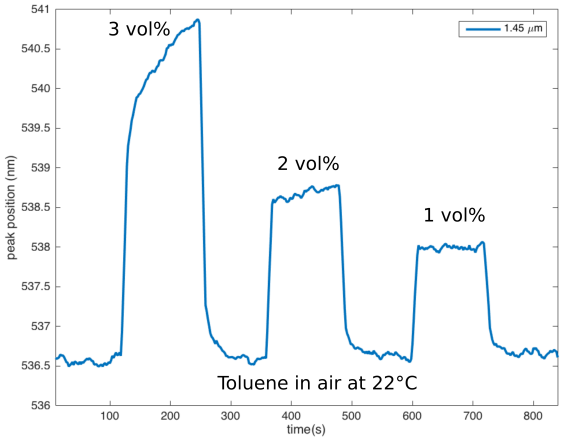

Figure 5.13. *Dynamic response of the resonance shift of sample 1.45 µm to different cycles of air/toluene at room temperature*

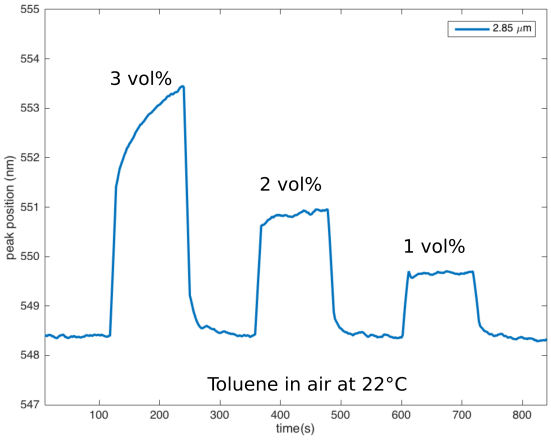

Figure 5.14. *Dynamic response of the resonance shift of sample 2.85 µm to different cycles of air/toluene at room temperature*

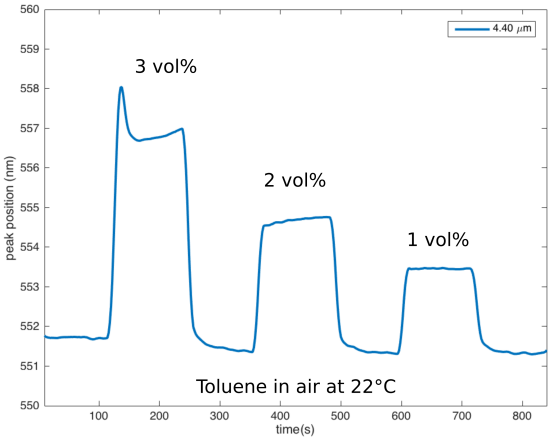

Figure 5.15. *Dynamic response of the resonance shift of sample 4.40 µm to different cycles of air/toluene at room temperature*

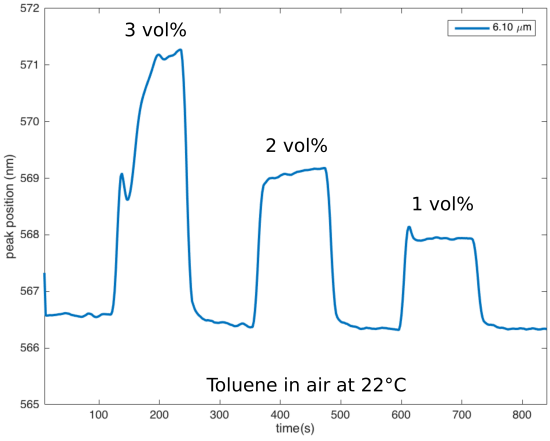

Figure 5.16. *Dynamic response of the resonance peak position of sample 6.10 µm to different cycles of air/toluene at room temperature*

Thickness [μm]	Concentration [vol %]	$\Delta\lambda_p$ [nm]
1.45	3	4.20
”	2	2.00
”	1	1.40
2.85	3	5.10
”	2	2.20
”	1	1.30
4.40	3	5.30
”	2	3.20
”	1	2.20
6.10	3	4.60
”	2	2.60
”	1	1.50

Table 5.3. Dynamic response of each sample to different >1 vol% concentrations of toluene

5.3.1 Low limit of detection

Same considerations as the previous results: all samples are able to detect up to 100 ppm, but the performances improve as the thickness increases, but if it increases too much then the gas molecule is not able to penetrate deeply in the cloud of TiO_2 and consequently not all the gold nanoparticles contribute to the overlall plasmonic resonance.

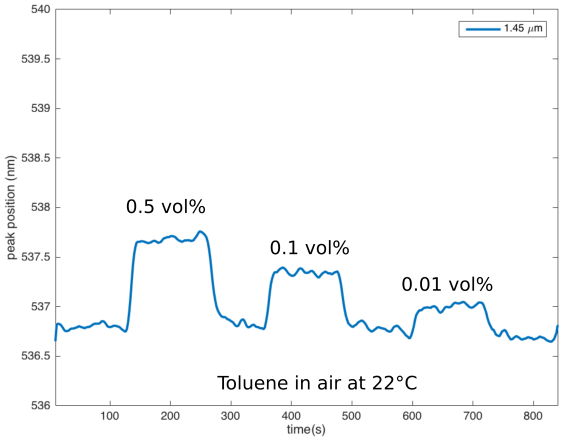

Figure 5.17. *Low limit of detection of sample 1.45 μm exposed toluene at room temperature*

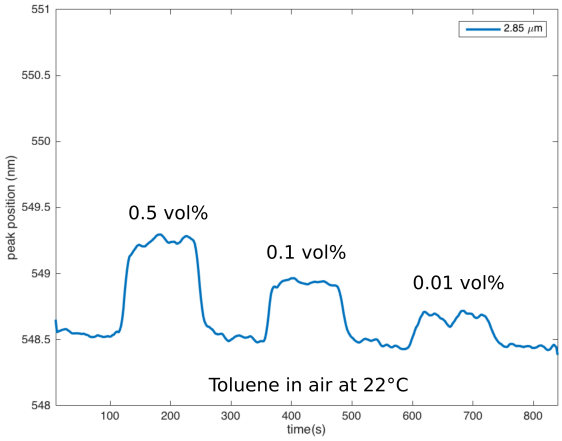

Figure 5.18. *Low limit of detection of sample 2.85 μm exposed to toluene at room temperature*

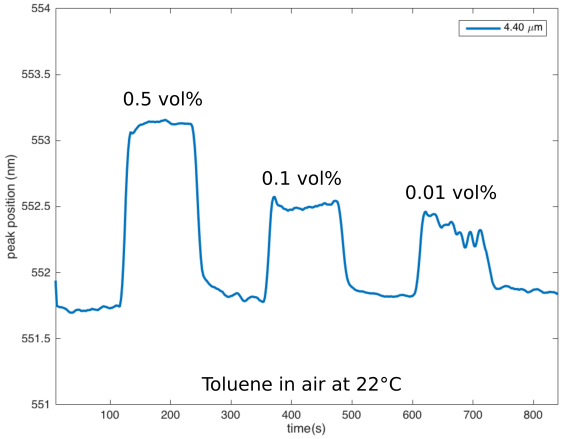

Figure 5.19. *Low limit of detection of sample 4.40 μm exposed to toluene at room temperature*

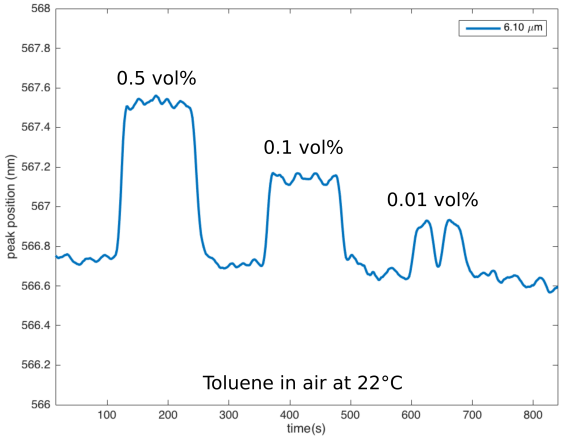

Figure 5.20. *Low limit of detection of sample 6.10 μm exposed to toluene at room temperature*

Thickness [μm]	Concentration [vol %]	$\Delta\lambda_p$ [nm]
1.45	0.5	0.70
”	0.1	0.50
”	0.01	0.30
2.85	0.5	0.75
”	0.1	0.55
”	0.01	0.40
4.40	0.5	1.40
”	0.1	0.85
”	0.01	0.70
6.10	0.5	0.80
”	0.1	0.50
”	0.01	0.30

Table 5.4. Dynamic response of each sample to different very low concentrations of toluene

5.4 Acetone

Acetone has formula $CH_3 - CO - CH_3$ and is an efficient biomarker for diagnosing diabetes, [17]. In this case, the interaction with the TiO_2 surface is likely to involve the carbonyl group (C-O). [10].
To have one more confirmation about what stated in the case of ethanol and toluene, another group of tests is performed with acetone (numerical results in Table 5.5): the results are still the same, with the only difference that all the samples show low shifts at 1 vol%, so a low limit of detection tests is not performed in this case. This is most probably due to the enthalpy of formation of acetone and some other intrinsic properties of acetone itself, which is high and consequently it gives low shifts, [10]

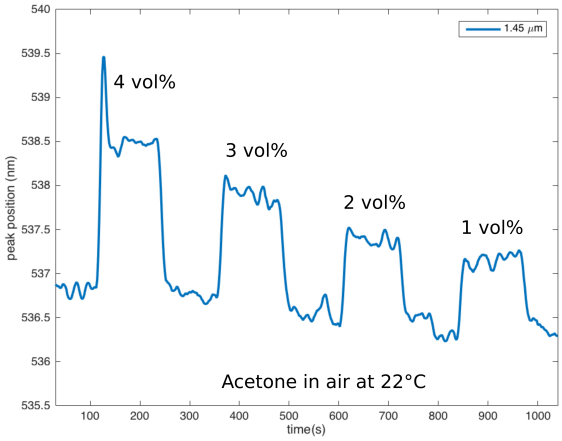

Figure 5.21. *Dynamic response of the resonance shift of sample 1.45 μm to different cycles of air/acetone at room temperature*

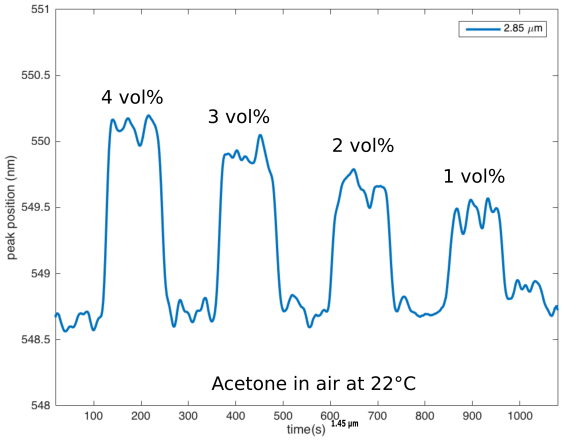

Figure 5.22. *Dynamic response of the resonance shift of sample 2.85 μm to different cycles of air/acetone at room temperature*

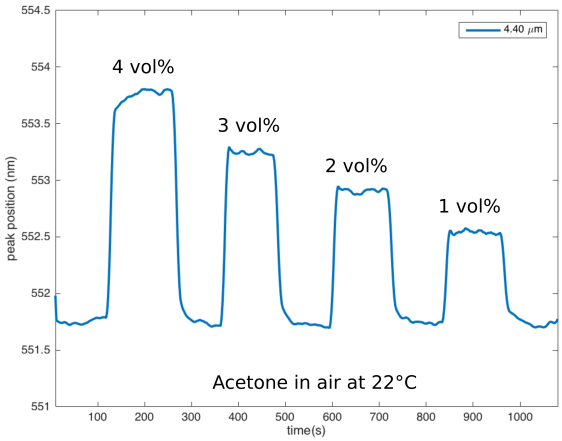

Figure 5.23. *Dynamic response of the resonance shift of sample 4.40 μm to different cycles of air/acetone at room temperature*

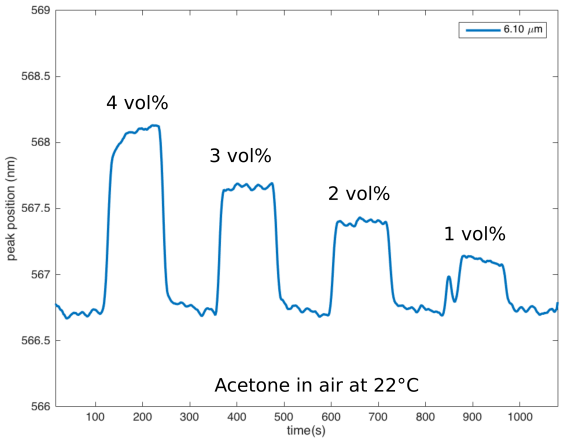

Figure 5.24. *Dynamic response of the resonance shift of sample 6.10 μm to different cycles of air/acetone at room temperature*

Thickness [μm]	Concentration [vol %]	$\Delta\lambda_p$ [nm]
1.45	4	1.40
”	3	1.30
”	2	1.10
”	1	0.80
2.85	4	1.50
”	3	1.40
”	2	1.20
”	1	0.90
4.40	4	1.90
”	3	1.50
”	2	1.30
”	1	1
6.10	4	1.70
”	3	1.40
”	2	0.90
”	1	0.50

Table 5.5. Dynamic response of each sample to different concentrations of acetone

5.5 Selectivity

In sections 5.2, 5.3 and 5.4 different cycles are performed and resonances shifts are shown. In order to be efficient a sensor should guarantee a good selectivity, which is the capability of the sensor to discern among different analytes. In other words, their responsivity must be identical given the same input, but different as the input changes. Otherwise users are not able to determine the presence of a gas rather than another. For this reason, please notice that each tested sensor has proven a great selectivity as each one react differently depending not only on the volatile compound, but also on the concentration values.
A simple and representative example is the plot in Figure 5.25: fixed the thickness of the Au/TiO_2 cluster, for each given gas (ethanol in dark blue, toluene in red, acetone in violet) and for a concentration

percentage ranging from 1 vol% to 4 vol%, the plasmonic shift increases (almost) linearly with the concentration.
This can be, for sure, a suitable and ideal property for safety applications, where an accurate discrimination of gases and concentrations are strictly required.

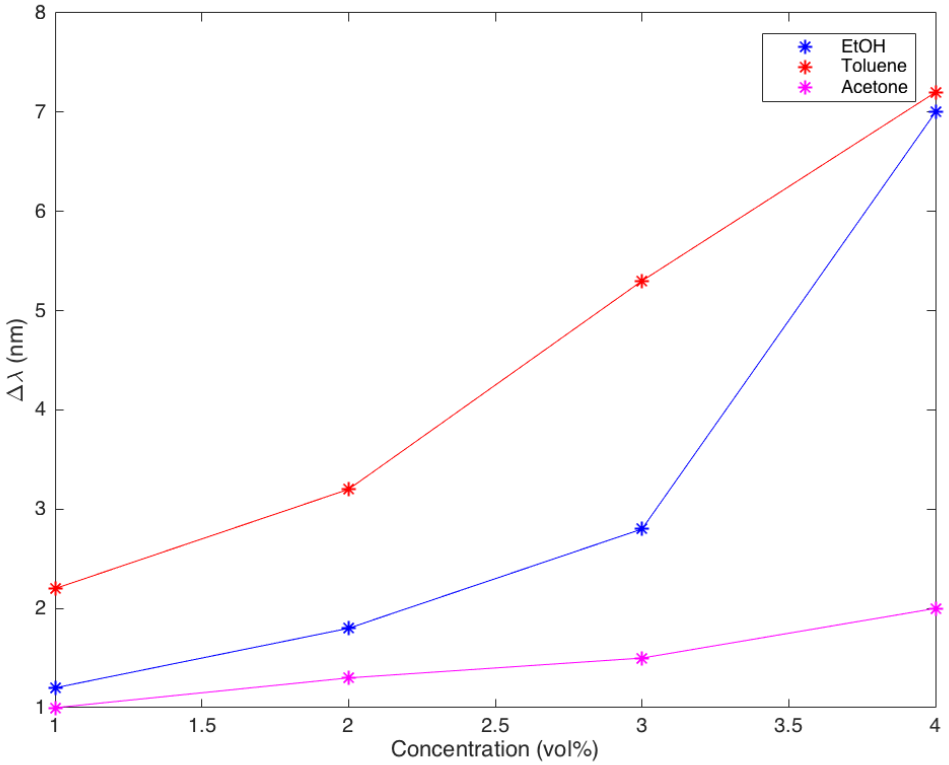

Figure 5.25. *Plasmonic shift of sample 4.40 μm to different gases at different concentrations*

5.6 Stability

Selectivity is not the only parameter to be considered, but also stability plays an important role to understand wether a sensor is performant or not: it is referred to the capability of the 4.40 μm sensor to show the same response even after a large amount of time. In this case only the low limit parameters are displayed, so only results with ethanol (Figure 5.26) and toluene (Figure 5.27) are compared, as acetone is not able to be detected at concentration lower than 1 vol%. In both plots the newest cycles (which are the same displayed in sections 5.2 and 5.3 and the ones from which final considerations are deducted) are drawn in blue, while the older simulations are in dashed red and, specifically, are 1 month old.
In Figure 5.26 the response seem to be unchanged even after this large amount of time, because the two lines tend to superpose one another: there is a small degradation when there is 0.5 vol% ethanol, but it can be considered negligible. There is also a little difference in correspondence of 0.01 vol% ethanol that is supposed to be due to the very low percentage of the gas itself, but also in this case the difference is so small that can be considered negligible.

In Figure 5.27 the superposition is not as precise as the previous one, but the final results are challenging as well: there is, indeed, a better response at 0.5 vol% and similar responses at 0.1 vol% and 0.01 vol%. For this reason, after all, one can conclude that the stability in time is very strong and make these sensors useful for a wide range of sensing applications.

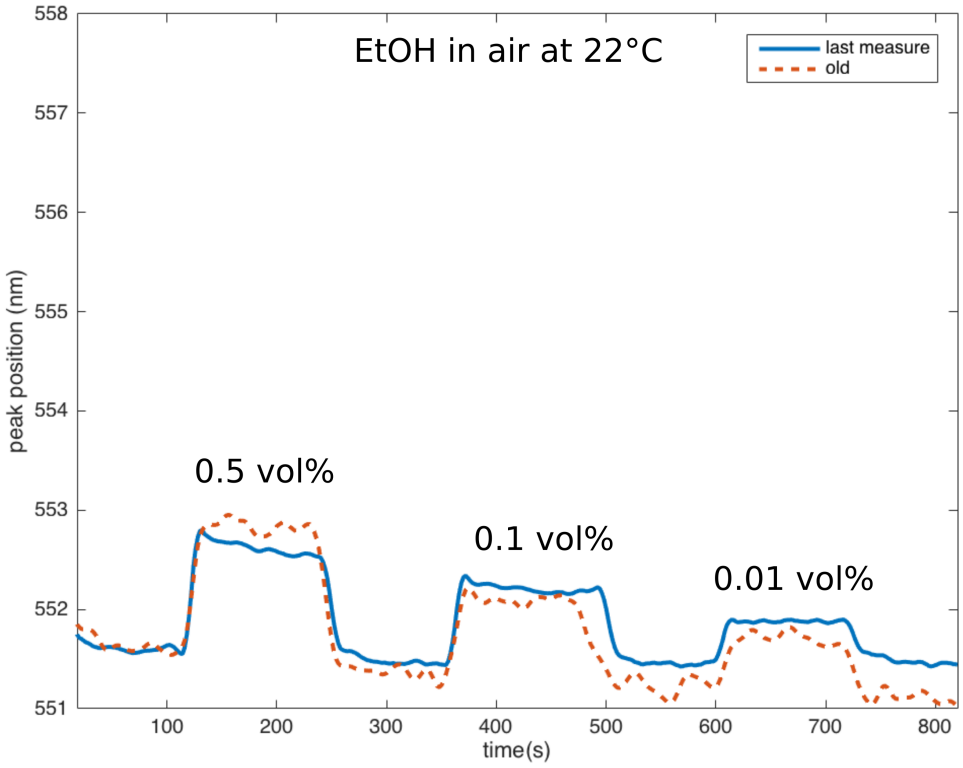

Figure 5.26. *Comparison between last measurements taken (in blue) and 1 month old measurements (dashed red line) of the resonance shift of sample 4.40 µm to different cycles of air/ethanol at room temperature*

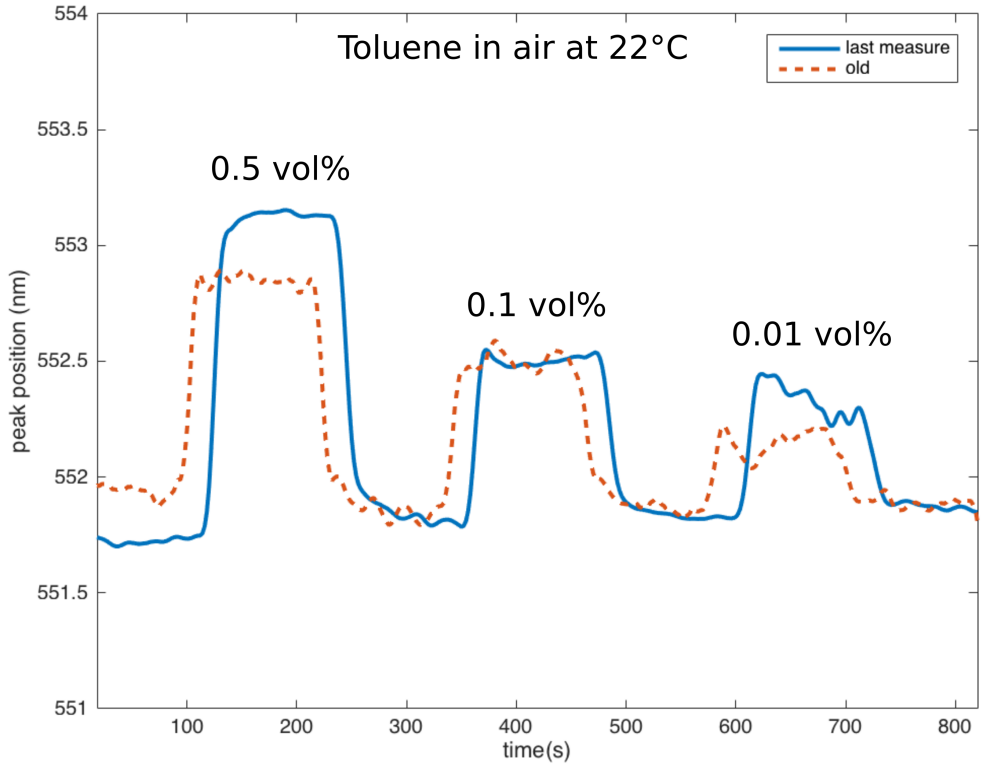

Figure 5.27. *Comparison between last measurements taken (in blue) and 1 month old measurements (dashed red line) of the resonance shift of sample 4.40 µm to different cycles of air/toluene at room temperature*

Chapter 6

Conclusion

In this work an all new plasmonic resonant architecture is fabricated through an innovative double flame synthesis process: a 3-dimensional cloud of TiO_2 with christalline Au nanoparticles inside. The advantage of having a 3D structure rather than a bilayer one has been seen clearly through enhancements in the electric field, thus in localized surface plasmon resonance. Consequently, visible sensing performances with metamaterials are possible.
From the results collected so far, a possible suggestion is to repeat the same sensing tests with other different volatile compounds and have an idea of selectivity and stability.
Another suggestion is acting on the optimization of the double flame setup (i. e. HAB and tilting angle), because double flame is not as common as single flame. By doing this there will be a possibility to fabricate more performant solutions and consequently a possibility to increase the sensitivity by reducing the low limit of detection.
By reducing the low limit of detection to less than 10 ppm, so that an accurate analysis of more complex systems such as the human breath should be possible. In this way metamaterials could be employed in hospitals for medical diagnostics or even as a lab-on-a-chip for detection of diseases.

Appendix A

Use of flame spray pyrolysys for Electrochromic WO_3 thin films

Due to many unexpected events that made the work on the main project stop for almost a month, the research group decided to focus on how to employ double flame aerosol synthesis and came out with the fabrication of electrochromic thin films made of WO_3. The main purpose of this Appendix is just to give a very quick idea of how promising and challenging this application can be, so just a preliminary analysis and characterization is carried out.

Introduction Flame spray pyrolysis is becoming a promising technique for highly porous films, and in this work the main focus is optical gas sensing. Another way to use it is also for electrochromism.
The main reasons to use electrochromic films are basically three: energy saving, due to the capability to control the solar heat circulation; safety purposes; open circuit memory, as it keeps the optical properties even when a bias is not applied, which is consequently connected to the energy saving purpose too. These purposes are not trivial, as nowadays it is important to avoid energy wasting and reducing pollution: with electrochromic smart glasses it is possible to achieve this

goal by managing the amount of heat and cold in a building, for example.

Electrochromism in WO_3 Electrochromism (EC) is an electro-optic property of some materials to change reversibly their optical properties when it is electrochemically reduced or oxidized, [33] or, in other words, when it is subject to an electric field. Electrochromism is normally shown through a color change between the transparent state and a colored state, or between two colored states. This color change is associated to insertion or extraction of cations (H^+ , Li^+ , Na^+) during a redox reaction from the electrolitic solution inside the host lattice of the EC working electrode layer.
Depending on this, it is possible to distinguish between two kind of materials: cathodic materials and anodic materials. Cathodic materials exhibit a coloration state at negative potential, meaning that they color when they are reduced (charge insertion), while anodic materials exhibit coloration at positive potential, meaning that they color when they are oxidized (charge extraction).

The first researcher who ever investigated on electrochromic cells and their behavior was Claes-Göran Granqvist in very early '00, [34]: according to him, the simplest electrochromic cell is a multi-layer device consisting of an active electrode layer, a counter electrode layer, an electrolyte layer separating the two electrodes, two transparent conducting layers serving as electrical leads, and the supporting substrates. The final structure is shown in Figure A.1. The two electrode layers often consist of transition metal oxides. In the off or bleached state, cations, such as Li^+ or H^+, reside in the electrolyte and the counter electrode. When the device is switched on, a voltage applied between the opposing conducting layers drives cations to

migrate from the counter electrode, through the electrolyte and into the electrochromic electrode through a Faradaic process, changing its oxidation state and its optical properties, [34]. [35]

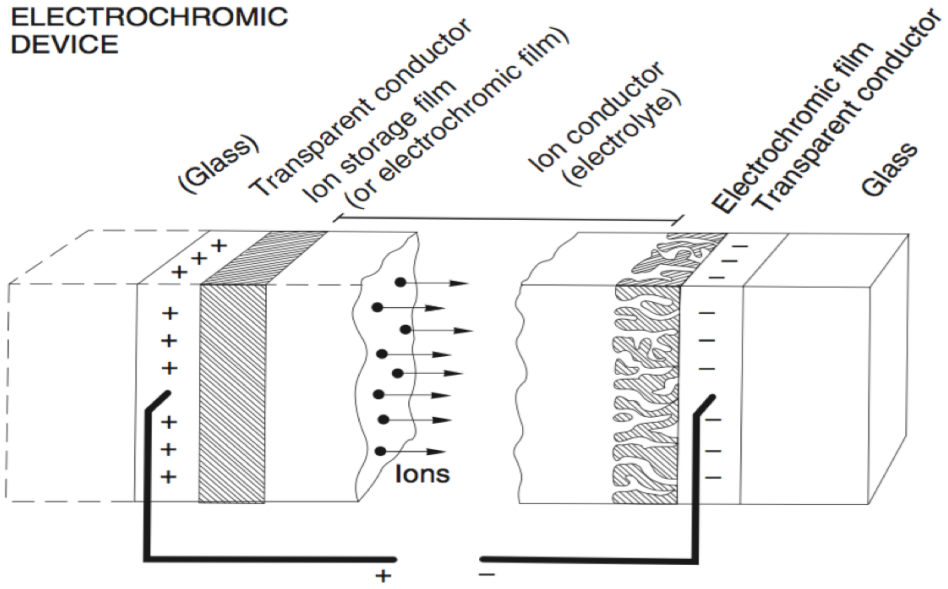

Figure A.1. *Simplest model of an electrochromic cell, [34]*

The most promising elechtrochromic materials are the so called transition materials, which exhibit good electrochromic properties in the visible and infrared region. The most versatile material is tungsten oxide (WO_3), as it exhibits large optical modulation, good durability, less stress for the viewer's eyes, and relatively low price with respect to other electrochromic materials, [33].

Most electrochromic oxides consist of octahedral units in various arrangements: these oxides are suitable both because of their electronic features and because the spaces between the octahedrals are sufficiently large to allow facile transport of small ions, [36].

Tungsten oxide has an octahedral structure, and the empty space available inside each octahedral can be filled by an interstitial atom. Figure A.2, in particular, illustrates nanostructural features of WO_3 and shows each octahedral consisting of one tungsten atom surrounded by six oxygen atoms. Each octahedron shares corners with neighbouring octahedral, so at the end 3D structure comprised by the octahedra yields to 3D 'tunnels' structure conducive for ion transport, [36]. This makes WO_3 a very appropriate electrochromic material as in interstitial sites the guest ions can be inserted and make transparency and coloration happen.

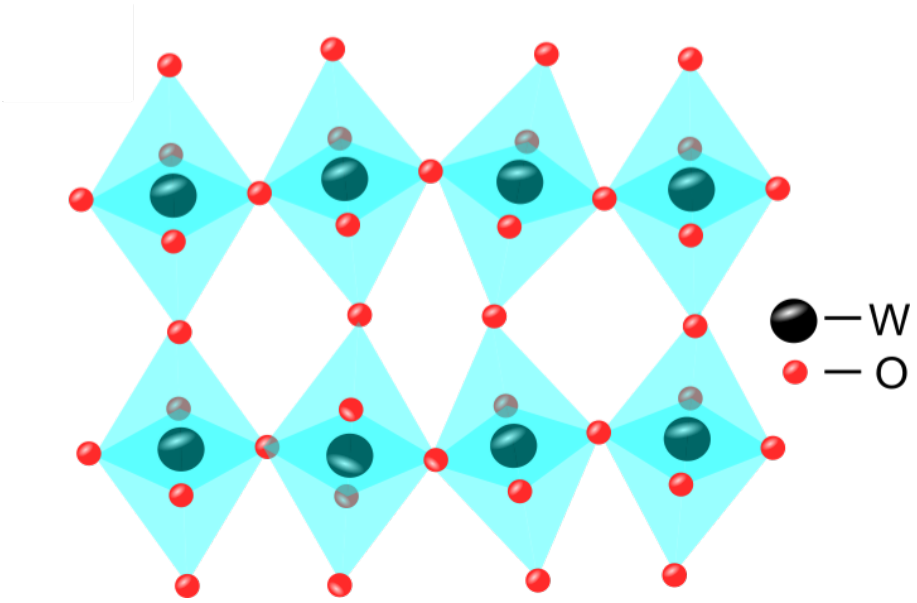

Figure A.2. *Model of the octahedral features in crystalline WO_3*

WO_3 thin films can be obtained through different methods, such as chemical bath deposition, [33], DC magnetron sputtering, [37], [39], or RF magnetron sputtering, [37], [38], sol-gel, [37], [40], but the exploitation of flame spray synthesis is still unexplored.

The electrochromic properties of WO_3 thin films to be computed are:

- Transmittance modulation (ΔT);
- Optical density (ΔOD);
- Coloration efficiency (η);
- Switching time (τ);

Each of them strongly depends on the structure and composition of the thin film, which depends directly on the deposition method and deposition conditions. Ideally one should obtain a high transmittance modulation, a high optical density, low coloration efficiency and a low switching time. In order to measure the electrochromic properties, a three-electrode cell is used: the sample is immersed in an electrolitic solution, in which a reference electrode and a counter electrode are immersed too (Figure A.3). The main goal is to investigate electrochromic properties and performances of WO_3 thin films by using flame spray pyrolysis.

Preparation Tungsten oxide films are deposited onto fluorine doped thin oxide (FTO) coated glass substrates. With aerosol flame synthesis three samples are fabricated, each one characterised by a different deposition time: 1s, 2s, 3s. Only the first two are tested for comparison.

Electrochemical characterization is performed with a three-electrode cell with WO_3 as working electrode: in case of H^+ intercalation 0.05M H_2SO_4 is used as electrolyte, Pt as counter electrode and Ag/AgCl as reference electrode.

$$(WO_3 + H^+ + e^-)_{transparent} \leftrightarrow (HWO_3)_{colored} \tag{A.1}$$

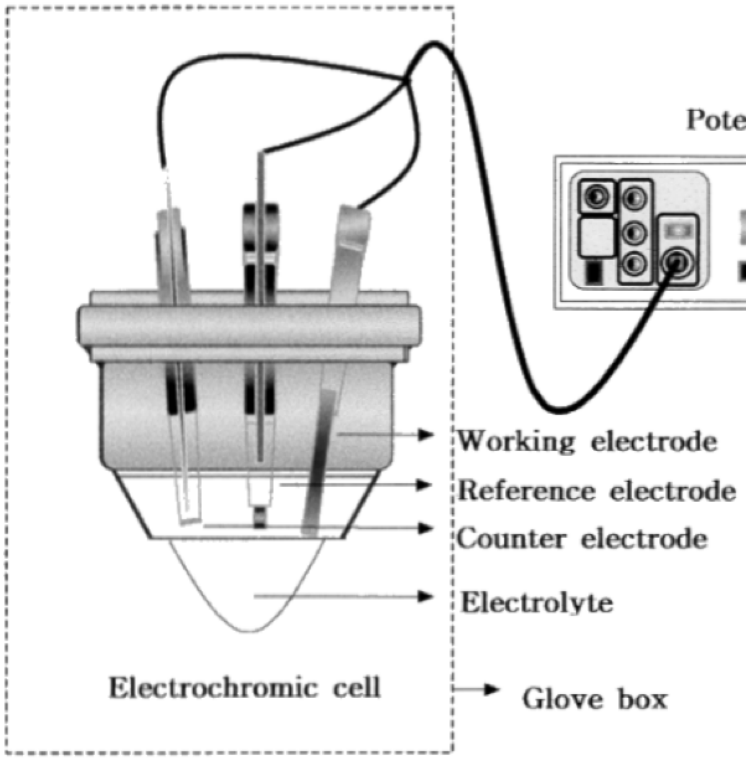

Figure A.3. *Experimental set up for voltammetry measurements on WO_3 film in an electrochromic cell, [41]*

The electrochromic cell is then biased at -0.5V/+0.5V and the results were taken after 150 cycles. The results turn out to be very challenging if one takes into account the very low bias to which the cell is supplied.

Characterization The crystallographic structure of the prepared samples is determined by using an X-ray diffractometer (XRD) equipped with CuKα radiation of average wavelength $\lambda = 1.54059$ Å in the range of 20 to 60. Figure A.4 is, thus, the XRD pattern of all the three as-deposited samples, in which it is possible to notice the typical γ- and ϵ-oriented octaedral structure. Specifically, in all of them sharp peaks related to FTO substrate are visible, then for 1s sample

monoclinic $\epsilon - WO_3$ peaks appear at 23.4°, 34.0° and 42.1°, while in the other two there are monoclinic $\gamma - WO_3$ peaks, according to [42], [43], [44]. This change can be attributed to the deposition time which suggests a transformation from one monoclinic orientation to another. In addition diffraction peaks seem to be sharper and higher, indicating an increasing crystal structure. Also, no hydrated WO_3 is found, indicating the purity of the WO_3 obtained, [43].
Particle sizes of each sample is calculated using the Scherrer equation and are equal to 12.9 nm for 1s sample, 18.9 nm for 2s and 20 nm for 3s samples respectively: thus, the crystallite size increases as the deposition time increases.

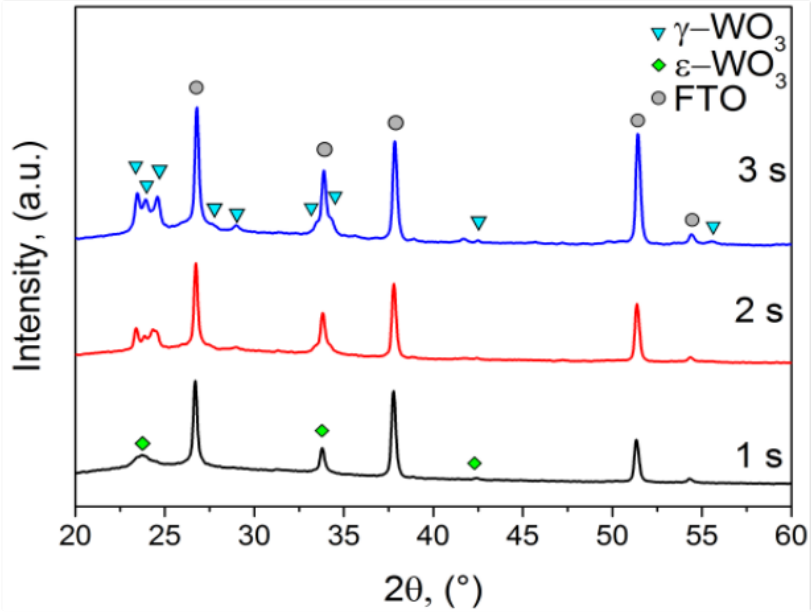

Figure A.4. *XRD patterns of the three electrochromic samples with different deposition times*

In order to evaluate the chemical bonding and molecular structure of the sample, an FTIR (Fourier transform infrared) spectra of the pure WO_3 is shown in Figure A.5. There is a broad band observed in the range of 3500-2500 cm^{-1} supposedly due to W-OH stretching bonds, while other two important bands are observed in the range of 1350 cm^{-1} due to W-OH$\cdots OH_2$ bending vibrations and around 750 cm^{-1} due to O-W-O stretching vibrations modes or the absorbed water molecules, according to [44] and [45]. So the FTIR results confirmed the presence of WO_3 phase with crystalline nature, [45].

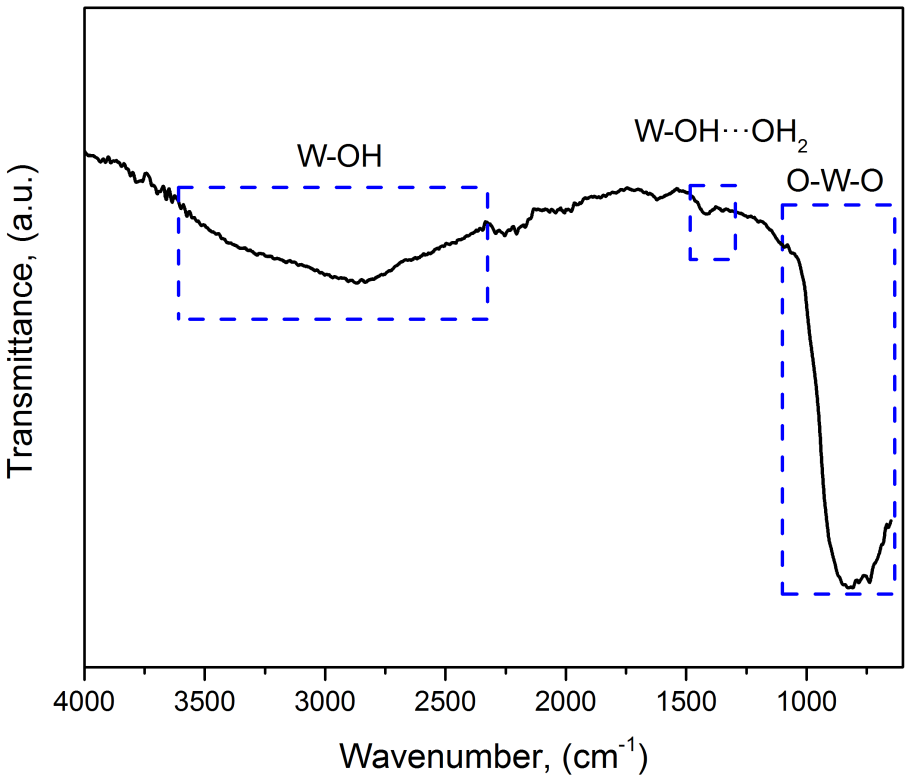

Figure A.5. *FTIR analysis of one WO_3 sample after being tested for some cycles*

Results For a real evaluation of the performances of the flame-made WO_3 smart glasses, some plots have been carried out. In particular those plots are related to the same parameters that were mentioned previously in the introduction (i. e. transmittance modulation, optical density, coloration efficiency, switching time). The optical modulation is set to 633 nm.
Generally speaking, the electrochromic performance of tungsten oxide films is affected by several factors including crystallinity, microstructure and surface morphology: the more the crystallinity is high, the higher electrochromic performances are possible, [46].
The main purpose is to get, in this very preliminary results, enhanced performances in these flame-made WO_3 thin films rather than otherwise synthesised WO_3.

- **Transmittance modulation ΔT**: it measures how much, at a certain wavelength (in this case 633 nm), the electrochromic film is able to change from a transparent (higher values of transmittance) to a colored state (lower values of transmittance) and viceversa from the same amount. Figure A.6 compares the transmittance of the samples obtained with 1s and 2s of deposition: please notice that both are very stable because the variation in transmittance never reduces, but please notice that in the 2s sample the modulation is about 40%, while in 1s is nearly 30%.

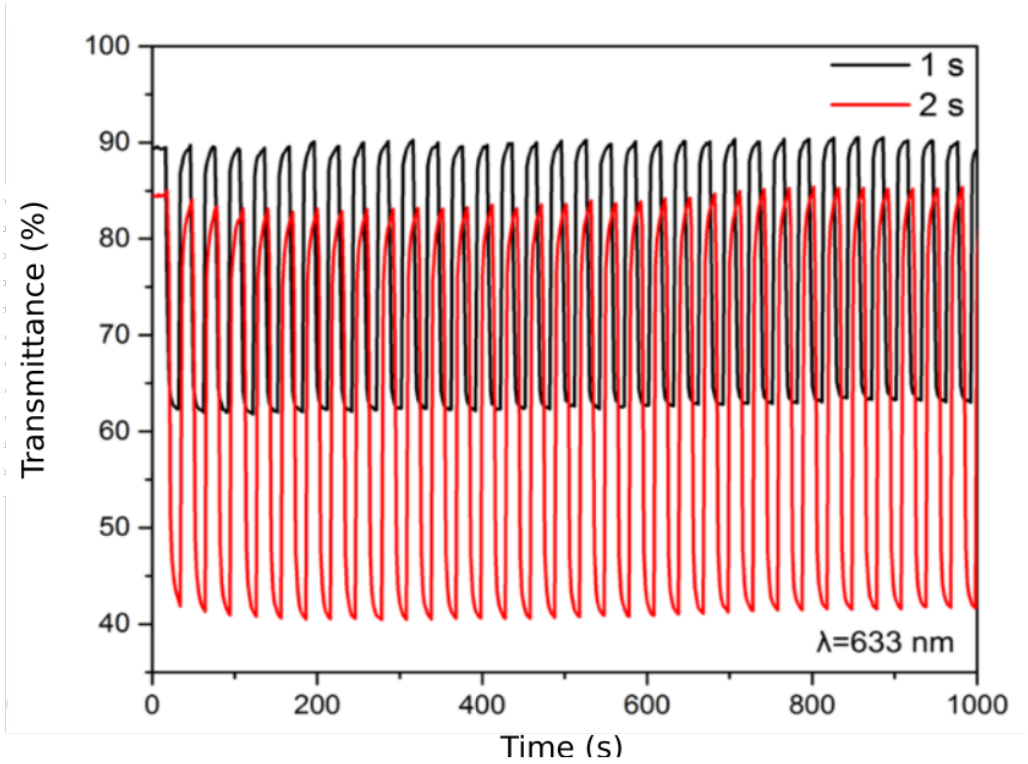

Figure A.6. *Transmittance modulation at 633 nm of WO_3 thin films in the bleached and colored states*

- **Optical density (ΔOD)** and **Coloration efficiency (η)**: they are shown in Figure A.7 as they are strictly related. Optical density is defined as the ratio between the transmittance in bleached and colored states, respectively:

$$\Delta OD = log\frac{T_b}{T_c} \tag{A.2}$$

while colouration efficiency at a given wavelength is defined as the variation of the optical density (ΔOD) divided by the charge (Q):

$$\eta = \frac{\Delta OD}{\Delta Q} \tag{A.3}$$

From Equation A.3 it turns out that if one plots the optical density as a function of the charge density (just like Figure A.7), then the colouration efficiency is basically the slope of the line fitted to the linear region of the curve, [33].
Generally, a high value of CE indicates that the electrochromic material exhibits a large optical modulation with a small intercalated (or extracted) charge density. Thus, this is why 2s sample shows a better performance according to the final results.

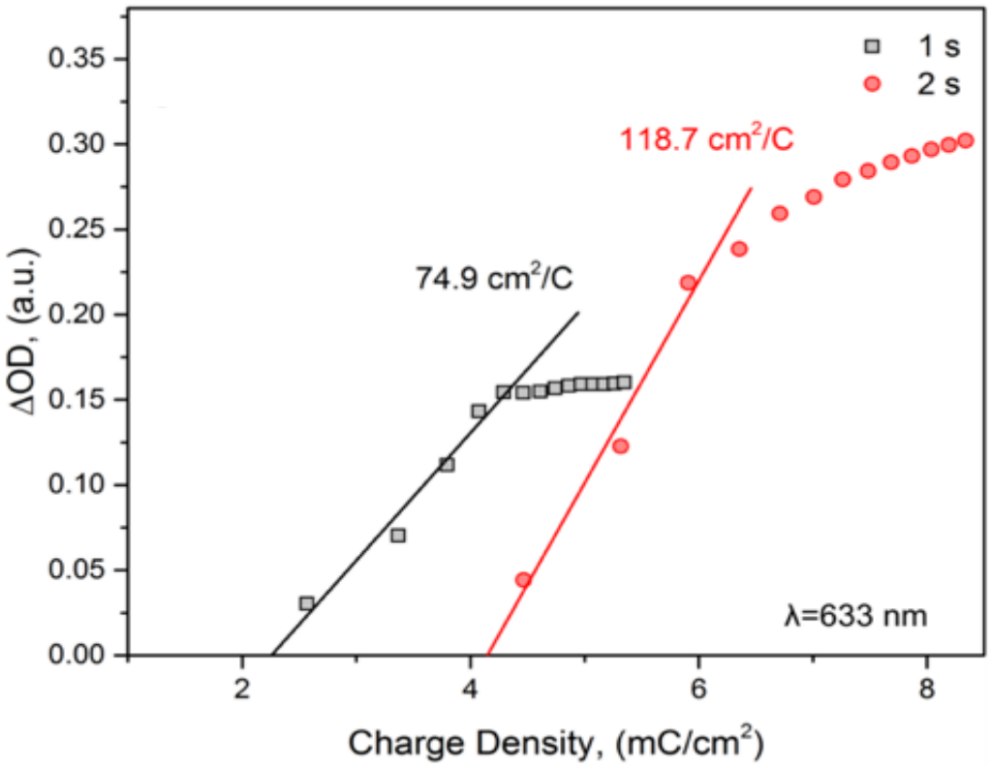

Figure A.7. *Optical density variation with respect to the charge density measured at 633 nm*

- **Switching time** (τ): it measures the reactivity of the electrochromic material, so in other words the capability to shift from a colored state to a transparent one (bleaching time or recovery time τ_{rec}) and viceversa (colouration time or response time τ_{res}).

The colouration and bleaching times are defined as time required for achieving 90 % of the total transmission change, and they are shown in Figure A.8. The applied potential is switched between 0.5 V (transparent state) and -0.5 V (blue state).
In both samples the colouration time is slower than the bleaching one but, surprisingly, it turns out that even if the 2s samples has proven to be better than the other one, its time swings are higher than the other.

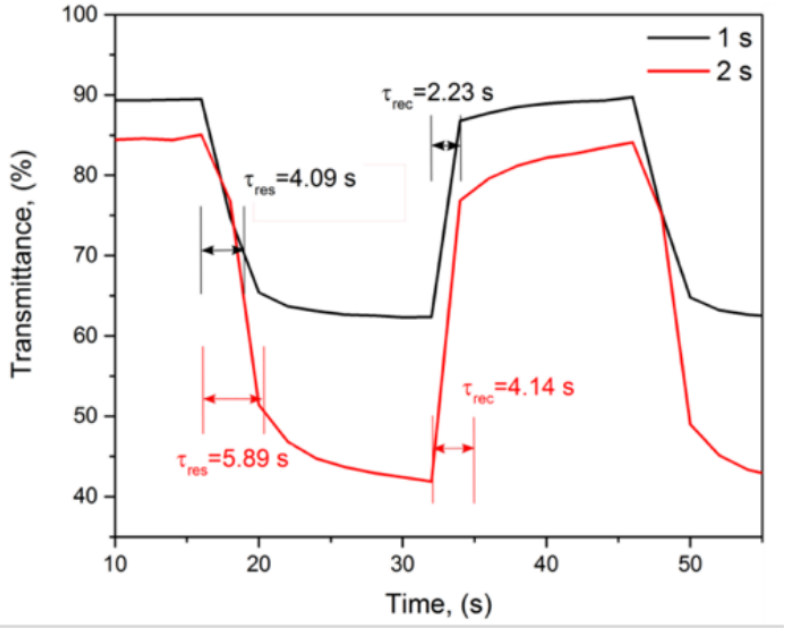

Figure A.8. *Dynamic colouration/bleaching switching times at a wavelength of 633 nm*

Comparison According to these results, a first distinction is possible among performances of WO_3 thin films fabricated with different methods. This comparison is shown in Table A.1, according to [40] (sol gel),[47] (evaporation), [48] (sputtering) and on this work (flame) respectively:

Deposition	Analyte,Voltage [V]	ΔT [%] @ λ [nm]	η [cm^2/C]	τ_{res} [s]/τ_{rec} [s]
Sol gel	0.5M H_2SO_4,-0.7/+1	50 @ 633	62	5/7
Evaporation	0.1M H_2SO_4,-1/+2	45 @ 550	32	3.8/14.05
Sputtering	0.1M $LiClO_4$,-1/+1	41 @ 630	10	17.35/11.75
Flame	0.05M H_2SO_4,-0.5/+0.5	30 @ 633	74.9	4.09/2.23
Flame	0.05M H_2SO_4,-0.5/+0.5	45 @ 633	118.7	5.89/4.14

Table A.1. Comparison with other synthesis methods

Conclusion In this preliminary work a purely crystalline monoclinic WO_3 thin film is fabricated through flame aerosol synthesis. After some tests on the main parameters a small comparison with other synthesis methods is possible: flame-made electrochromic cells exhibit a larger optical modulation with a small charge density and are generally fast. Transmittance modulation is still poor, but in conclusion these are challenging results as it required much less analyte concentration with respect to other deposition methods together with the lowest bias voltage required.
For the future an investigation on reducing this ΔT so that a total change from colour to transparent state would be possible, and then proceed with some more optimization even on the flame setup as this fabrication method is still very new.

Bibliography

[1] Jing Zhao, Xiaoyu Zhang, Chanda Ranjit Yonzon, Amanda J. Haes, Richard P. Van Duyne, *Localized surface plasmon resonance biosensors*, 2006, Nanomedicine, pp. 219-228

[2] Kathryn M. Mayer, and Jason H. Hafner *Localized Surface Plasmon Resonance Sensors*, 2011, Chemical Reviews, pp. 3828-3857

[3] S.P. Yushanov, L.T. Gritter, J.S. Crompton and K.C Koppenhoefer, *Surface Plasmon Resonance*, 2012, 2012 COMSOL Conference in Boston, pp. 1-6

[4] Neha Nehru, *Reference Compensation for Localized Surface- Plasmon Resonance Sensors*, 2014, UKnowledge, pp. 1-157

[5] Giovanni Ghione, *Photonic waveguides*, 2017, Politecnico di Torino, Microwave & RF Electronics Group, pp. 1-64

[6] Andreas Otto, *Excitation of Nonradiative Surface Plasma Waves in Silver by the Method of Frustrated Total Reflection*, 1968, Zeitschrift für Physik 216, pp. 398-410

[7] E. Kretschmann and H. Raether, *Radiative Decay of Non Radiative Surface Plasmons Excited by Light*, 1968, Z. Naturforsch 23a, pp. 2135-2136

[8] William L. Barnes, Alain Dereux and Thomas W. Ebbesen, *Surface plasmon subwavelength optics*, 2003, Nature 424, pp. 824-830

[9] Longhua Guoa, Joshua A. Jackmanb, Huang-Hao Yangd, Peng Chena, Nam-Joon Choa, Dong-Hwan Kim, *Strategies for enhancing the sensitivity of plasmonic nanosensors*, 2015, Nano Today, pp.

213-239

[10] Zelio Fusco, Mohsen Rahmani, Renheng Bo, Ruggero Verre, Nunzio Motta, Mikael Käll, Dragomir Neshev, and Antonio Tricoli, *Nanostructured Dielectric Fractals on Resonant Plasmonic Metasurfaces for Selective and Sensitive Optical Sensing of Volatile Compounds*, 2018, Advanced Materials, pp. 1-11

[11] K. Lance Kelly, Eduardo Coronado, Lin Lin Zhao, and George C. Schatz, *The Optical Properties of Metal Nanoparticles: The Influence of Size, Shape, and Dielectric Environment*, 2003, American Chemical Society, pp. 668-677

[12] Nina Jiang, Xiaolu Zhuo, and Jianfang Wang, *Active Plasmonics: Principles, Structures,and Applications*, 2018, Chemical Reviews, pp. 3054-3099

[13] Jeffrey N. Anker, W. Paige Hall, Olga Lyandres, Nilam C. Shah, Jing Zhao and Richard P. Van Duyne, *Biosensing with plasmonic nanosensors*, 2014, Nature Publishing Group, pp. 442-453

[14] Antonio Tricoli, Marco Righettoni, and Alexandra Teleki, *Semiconductor Gas Sensors: Dry Synthesis and Application*, 2010, Angenwandte Chemie, pp. 7632-7659

[15] Bin Chen, Chuanjun Liu, Lingpu Ge, Kenshi Hayashi, *Localized surface plasmon resonance gas sensor of Au nano-islands coated with molecularly imprinted polymer: Influence of polymer thickness on sensitivity and selectivity*, 2016, Elsevier, pp. 787-792

[16] Andreas Tittl, Harald Giessen and Na Liu, *Plasmonic gas and chemical sensing*, 2014, Nanophotonics, pp. 157-180

[17] Antonio Tricoli, Noushin Nasiri, and Sayan De, *Wearable and Miniaturized Sensor Technologies for Personalized and Preventive Medicine*, 2017, Advanced Functional Materials, pp. 1-19

[18] Marco Righettoni and Antonio Tricoli, *Toward Portable Breath Acetone Analysis for Diabetes Detection*, 2011, J Breath Res., pp.

1-16

[19] Gang Peng, Ulrike Tisch, Orna Adams, Meggie Hakim, Nisrean Shehada, Yoav Y. Broza, Salem Billan, Roxolyana Abdah-Bortnyak, Abraham Kuten and Hossam Haick, *Diagnosing lung cancer in exhaled breath using gold nanoparticles*, 2009, Nature Nanotechnology, pp. 669-673

[20] Austin Fox, *Derivation of FWHM and Height for Peak Fitting Functions*, http://openafox.com/science/peak-function-derivations.html#exponential-gaussian, Last Edit: 29 Nov 2017

[21] Wey Yang Teoh, Rose Amal and Lutz Mädler, *Flame spray pyrolysis: An enabling technology for nanoparticles design and fabrication*, 2010, Nanoscale, pp. 1324-1347

[22] Reto Strobel, Lutz Mädler, Marco Piacentini, Marek Maciejewski, Alfons Baiker, and Sotiris E. Pratsinis, *Two-Nozzle Flame Synthesis of $Pt/Ba/Al_2O_3$ for NO_x Storage*, 2006, Chemical Materials, pp. 2532-2537

[23] Antonio Tricoli, Noushin Nasiri, Hongjun Chen, Anna S. Wallerand, Marco Righettoni, *Ultra-rapid synthesis of highly porous and robust hierarchical ZnO films for dye sensitized solar cells*, 2016, Solar Energy, pp. 553-559

[24] H. K. Grossmann, A. Gröhn, F. Meierhofer, U. Fritsching, K. Wegner, L. Mädler, *Experimental characterization of the Double Flame Spray Pyrolysis Process based on the deposition of Pt on a TiO_2 support*, 2014, Aerosol Technology 2014, Abstract T111A01

[25] J A Kemmler et al, *Flame spray pyrolysis for sensing at the nanoscale*, 2013, Nanotechnology, pp. 1-14

[26] Antonio Tricoli, Markus Graf, Felix Mayer, Stéphane Kühne, Andreas Hierlemann, and Sotiris E. Pratsinis, *Micropatterning Layers by Flame Aerosol Deposition-Annealing*, 2008, Advanced Materials, pp. 3005-3010

[27] Noushin Nasiri, Anthony Ceramidas, Shayanti Mukherjee, Anitha Panneerselvan, David R. Nisbet and Antonio Tricoli, *Ultra-Porous Nanoparticle Networks: A Biomimetic Coating Morphology for Enhanced Cellular Response and In ltration*, 2016, Scientific Reports, pp. 2-11

[28] M. Minnermann, H.K. Grossmann, S. Pokhrelb, K. Thielc, H. Hagelin-Weaverd, M. Bäumera, L. Mädler, *Double flame spray pyrolysis as a novel technique to synthesize alumina-supported cobalt Fischer–Tropsch catalysts*, 2013, Catalysis today, pp. 90-99

[29] Gian Luca Chiarello, Elena Selli, Lucio Forni, *Photocatalytic hydrogen production over flame spray pyrolysis-synthesised TiO_2 and Au/TiO_2*, 2008, Applied Catalysis B: Environmental, pp. 332-339

[30] Wey Yang Teoh, Rose Amal, Lutz Mädler, Sotiris E. Pratsinis, *Flame sprayed visible light-active Fe-TiO_2 for photomineralisation of oxalic acid*, 2007, Catalysis Today 120, pp. 203–213

[31] Noushin Nasiri, Renheng Bo, Tak Fu Hung, Vellaisamy A. L. Roy, Lan Fu, Antonio Tricoli, *Tunable Band-Selective UV-Photodetectors by 3D Self-Assembly of Heterogeneous Nanoparticle Networks*, 2016, Advanced Functional Materials, pp. 7359-7366

[32] Andreas B. Dahlin, Jonas O. Tegenfeldt, and Fredrik Höök, *Improving the Instrumental Resolution of Sensors Based on Localized Surface Plasmon Resonance*, 2006, American Chemical Society, pp. 4416-4423

[33] Julijana Velevska, Nace Stojanov, Margareta Pecovska-Gjorgjevich, Metodija Najdoski, *Electrochromism in tungsten oxide thin films prepared by chemical bath deposition*, 2017, J. Electrochem. Sci. Eng., pp. 27-37

[34] Claes-Göran Granqvist, *Handbook of Inorganic Electrochromic Oxides*, 1995, Elsevier, Amsterdam

[35] Evan L. Runnerstrom, Anna Llordés, Sebastien D. Lounis and

Delia J. Milliron, *Nanostructured electrochromic smart windows: traditional materials and NIR-selective plasmonic nanocrystals*, 2014, Chem. Commun., pp. 10555-10572

[36] Claes-Göran Granqvist, *Electrochromic Metal Oxides: An Introduction to Materials and Devices*, 2015, Wiley-VCH Verlag GmbH & Co. KGaA, pp. 3-40

[37] Vyomesh R. Bucha, Amit Kumar Chawlab, Sushant K Rawal, *Review on electrochromic property for WO_3 thin films using different deposition techniques*, 2016, Materials Today: Proceedings 3, pp. 1429-1437

[38] Vempuluri Madhavi, Paruchuri Kondaiah, Obili Mahammad Hussain, and Suda Uthanna, *Structural, Optical, and Electrochromic Properties of Pure and Mo-Doped WO_3 Films by RF Magnetron Sputtering*, 2013, Hindawi, pp. 1-5

[39] Miguel Arvizu, Claes-Göran Granqvist and Gunnar Niklasson, *Electrochromism in sputter deposited $W_{1-y}Mo_yO_3$ thin films*, 2016, Journal of Physics: Conference Series 682 012005

[40] G.F. Cai, J.P. Tu, D. Zhou, X.L. Wang, C.D. Gu, *Growth of vertically aligned hierarchical WO3 nano-architecture arrays on transparent conducting substrates with outstanding electrochromic performance*, 2014, Solar Energy Materials & Solar Cells, pp. 103-110

[41] Kil Dong Lee, *Influence of Film Thickness on the Chemical Stability of Electrochromic Tungsten Oxide Film*, 2000, Journal of the Korean Physical Society, pp. 33-37

[42] Wenzhang Li, Jie Li, Xuan Wang, Jun Ma, Qiyuan Chen, *Photoelectrochemical and physical properties of WO_3 films obtained by the polymeric precursor method*, 2010, Internation Journal of Hydrogen Energy, pp. 13137-13145

[43] S. Poongodi, P. Suresh Kumar, Yoshitake Masuda, D. Mangalaraj, N. Ponpandian, C. Viswanathana and Seeram Ramakrishna, *Synthesis of hierarchical WO_3 nanostructured thin films with enhanced electrochromic performance for switchable smart windows*, 2015, Royal Society of Chemistry, pp. 96416-96427

[44] Yanbai Shen, Wei Wang, Xiangxiang Chen, Baoqing Zhang, Dezhou Wei, Shuling Gao and Baoyu Cui, *Nitrogen dioxide sensing using tungsten oxide microspheres with hierarchical nanorod-assembled architectures by a complexing surfactant-mediated hydrothermal route*, 2016, Royal Society of Chemistry, pp. 1345-1352

[45] S. Ramkumar, G. Rajarajan, *Effect of Fe doping on structural, optical and photocatalytic activity of WO3 nanostructured thin films*, 2016, Mater Sci: Mater Electron, pp. 1847-1853

[46] Chun-Kai Wang, Chung-Kwei Lin, Ching-Lin Wu, Sanjaya Brahma, Sheng-Chang Wang, Jow-Lay Huang, *Characterization of electrochromic tungsten oxide film from electrochemical anodized RF-sputtered tungsten films*, 2013, Ceramics International, pp. 4293-4298

[47] Ayat Esmail, Hany Hashem, Soltan Soltan, Mahmoud Hammam, and Ahmed Ramadan, *Thickness dependence of electro-optical properties of WO_3 films as an electrochromic functional material for energy-efficient applications*, 2017, Physica Status Solidi, pp. 2-9

[48] Ö. Tuna, A. Sezgin, R. Budakoglu, S. Türküz, H. Parlar, *Electrochromic properties of tungsten trioxide (WO_3) layers grown on ITO/glass substrates by magnetron sputtering*, 2015, Vacuum, pp. 28-31